Acta Pharmacologica Sinica

www.nature.com/aps

ARTICLE

Cytosolic DNA initiates a vicious circle of aging-related endothelial inflammation and mitochondrial dysfunction via STING: the inhibitory effect of Cilostazol

Zhi-hua Zheng[1,2,3,4], Jiao-jiao Wang[1,2], Jiu-guo Lin[1,2], Wei-le Ye[1,2], Jia-mi Zou[1,2], Li-yin Liang[3], Ping-lian Yang[1,2], Wan-lu Qiu[1,5], Yuan-yuan Li[1,2], Si-jia Yang[6], Man Zhao[7,8], Qing Zhou[5], Cheng-zhi Li[9], Min Li[3,4], Zhuo-ming Li[3], Dong-mei Zhang[1,2], Pei-qing Liu[3,4]✉ and Zhi-ping Liu[1,2]✉

Endothelial senescence, aging-related inflammation, and mitochondrial dysfunction are prominent features of vascular aging and contribute to the development of aging-associated vascular disease. Accumulating evidence indicates that DNA damage occurs in aging vascular cells, especially in endothelial cells (ECs). However, the mechanism of EC senescence has not been completely elucidated, and so far, there is no specific drug in the clinic to treat EC senescence and vascular aging. Here we show that various aging stimuli induce nuclear DNA and mitochondrial damage in ECs, thus facilitating the release of cytoplasmic free DNA (cfDNA), which activates the DNA-sensing adapter protein STING. STING activation led to a senescence-associated secretory phenotype (SASP), thereby releasing pro-aging cytokines and cfDNA to further exacerbate mitochondrial damage and EC senescence, thus forming a vicious circle, all of which can be suppressed by STING knockdown or inhibition. Using next-generation RNA sequencing, we demonstrate that STING activation stimulates, whereas STING inhibition disrupts pathways associated with cell senescence and SASP. In vivo studies unravel that endothelial-specific *Sting* deficiency alleviates aging-related endothelial inflammation and mitochondrial dysfunction and prevents the development of atherosclerosis in mice. By screening FDA-approved vasoprotective drugs, we identified Cilostazol as a new STING inhibitor that attenuates aging-related endothelial inflammation both in vitro and in vivo. We demonstrated that Cilostazol significantly inhibited STING translocation from the ER to the Golgi apparatus during STING activation by targeting S162 and S243 residues of STING. These results disclose the deleterious effects of a cfDNA-STING-SASP-cfDNA vicious circle on EC senescence and atherogenesis and suggest that the STING pathway is a promising therapeutic target for vascular aging-related diseases.

Keywords: cilostazol; STING; endothelial cell senescence; inflammation; mitochondrial dysfunction; atherosclerosis

Acta Pharmacologica Sinica (2024) 0:1–19; https://doi.org/10.1038/s41401-024-01281-0

INTRODUCTION

Endothelial cells (ECs) are regularly arranged in the vascular cavity and cover the entire circulatory system. As a vital structure of the vascular system, ECs have the functions of regulating vascular permeability and vascular tension, maintaining blood flow, and regulating neovascularization [1]. As they play a crucial role in maintaining vascular homeostasis, alterations of ECs are directly involved in a broad spectrum of vascular diseases, especially atherosclerosis [2, 3]. Vascular aging is a prevalent consequence of the aging of vascular ECs and smooth muscle cells (VSMCs), which is the underlying cause of numerous chronic inflammatory diseases in the elderly population. As the barrier layer between blood and vascular tissues, ECs are effector organs that perceive and respond to external stimuli. Consequently, aging especially causes greater DNA damage and telomere dysfunction in vascular ECs compared with VSMCs [4, 5]. EC senescence further induces changes in vascular structure and dysfunction, such as enhancing vascular inflammation and mitochondrial dysfunction, obstructing angiogenesis, affecting vascular integrity, thereby inducing or aggravating vascular aging, and promoting the occurrence and development of related cardiovascular diseases (CVDs, such as atherosclerosis and hypertension) [6]. However, the mechanism of

[1]State Key Laboratory of Bioactive Molecules and Druggability Assessment, Jinan University, Guangzhou 510632, China; [2]Guangdong Province Key Laboratory of Pharmacodynamic Constituents of Traditional Chinese Medicine and New Drugs Research, College of Pharmacy, Jinan University, Guangzhou 510632, China; [3]Laboratory of Pharmacology & Toxicology, School of Pharmaceutical Sciences, Sun Yat-sen University, Guangzhou 510006, China; [4]National and Local United Engineering Lab of Druggability and New Drugs Evaluation, School of Pharmaceutical Sciences, Sun Yat-sen University, Guangzhou 510006, China; [5]Department of Ophthalmology, the First Affiliated Hospital, Jinan University, Guangzhou 510006, China; [6]Department of Hepatobiliary Surgery, Sun Yat-sen Memorial Hospital, Sun Yat-sen University, Guangzhou 510120, China; [7]School of Pharmaceutical Sciences, Shenzhen University Medical School, Shenzhen 518060, China; [8]Guangdong Key Laboratory for Biomedical Measurements and Ultrasound Imaging, National-Regional Key Technology Engineering Laboratory for Medical Ultrasound, School of Biomedical Engineering, Shenzhen University Medical school, Shenzhen 518060, China and [9]Department of Interventional Radiology and Vascular Surgery, The First Affiliated Hospital of Jinan University, Guangzhou 510006, China
Correspondence: Pei-qing Liu (liupq@mail.sysu.edu.cn) or Zhi-ping Liu (liuzhiping@jnu.edu.cn)
These authors contributed equally: Zhi-hua Zheng, Jiao-jiao Wang.

Received: 19 December 2023 Accepted: 28 March 2024
Published online: 30 April 2024

EC senescence has not been completely revealed, and so far, there is no specific medicine in the clinic to treat EC senescence and vascular aging. Therefore, it is essential to disclose the regulatory mechanisms and new therapeutic targets of vascular aging and further develop efficient and specific preventive and therapeutic drugs [7, 8].

Stimulator of interferon genes (STING), as a type of natural adapter protein that recognizes double-stranded DNA (dsDNA), is the core molecule of innate immunity; upon activation, it substantially promotes the release of interferon and inflammatory factors [9, 10]. Previous studies have shown that under pathological conditions such as aortic aneurysm and dissection, atherosclerosis, cell senescence, and vascular dysfunction, the amount of endogenous DNA exceeds the physiological threshold of tolerance, and the abnormal presence of cytoplasmic free DNA (cfDNA) becomes a damaging factor that exacerbates disease via the inflammatory effect [11–16]. Proper activation of STING is essential for anti-viral immunity and immune stimulation in tumor immunotherapy [17], but excessive activation of innate immunity may lead to autoimmune diseases and chronic inflammation, which are detrimental to cardiovascular and cerebrovascular health [13, 15]. Overactivated STING signaling has become a prerequisite for chronic inflammatory diseases and CVDs [13, 15, 16, 18, 19]. Meanwhile, the role of excess type I interferon (IFN) in vascular endothelial senescence is still unclear. It is also uncertain whether the ECs release cfDNA in response to various aging stimuli within the local microenvironments, which is the key factor that causes STING overactivation and aggravates aging-related inflammation and mitochondrial dysfunction.

Endothelial senescence is a cellular stress response initiated by molecular damage that causes permanent cell cycle arrest and elicits significant phenotypic alterations, including the generation of the biologically active secretion set known as the senescence-associated secretory phenotype (SASP) [20]. Senescent cells secrete many pro-inflammatory cytokines, proteases, growth factors, angiogenesis factors, and cfDNA, which destroy the microenvironment, damage tissue structure and function, and thus promote the development of local and systemic senescence related pathology [21]. However, it remains to be seen whether SASP induced by endothelial senescence, as an EC injury factor, will activate STING to up-regulate its downstream NF-κB and IRF3 pathways and, in turn, exacerbate endothelial senescence by releasing SASP factors, such as inflammatory factors, type I interferon β (IFNβ), and cfDNA.

In this study, we show that STING serves as the core and tie of a cfDNA-STING-SASP-cfDNA vicious circle to accelerate aging-related endothelial inflammation and mitochondrial dysfunction and promote the development of atherosclerosis. We also identify that Cilostazol, an FDA-approved vasoprotective drug, is able to suppress the STING pathway by targeting STING S162 and S243 sites and alleviate vascular endothelial inflammation and senescence. Our findings disclose a new link between innate immunity and EC senescence and suggest that the STING pathway holds great potential as a novel drug target against vascular aging-related diseases.

MATERIALS AND METHODS

Animals

The animal procedures used in this study were approved by the Sun Yat-sen University Institutional Animal Care and Use Committee. *Sting*$^{-/-}$ mice were generated by Cyagen Bioscience Inc. (Guangzhou, China). *Apoe*$^{-/-}$ mice were generated by the Jackson Laboratory (Cat. No. 002052). Experiments were conducted on both male and female mice, with littermates serving as controls. To knock down *Sting* in ECs, adeno-associated viruses (AAV) were obtained from Vigene Biosciences (Shandong, China) and delivered by tail vein injection. WT mice were injected with AAV containing the *shSting* coding sequence (5′-CAACATTC-GATTCCGAGATAT-3′) and GFP protein (AAV9-ICAM2-*shSting*-GFP-RGDLRVS), or control viruses only containing GFP protein (AAV9-ICAM2-GFP-RGDLRVS) using 5×10^{11} vg/mouse.

Drug-induced endothelial senescence in vivo

The mouse model of acute vascular endothelial senescence in vivo follows the previously described protocol [22, 23]. Briefly, eight-week-old mice were single intraperitoneally injected with equal amounts of saline or paraquat (1,1-dimethyl-4,4-bipyridinium, Sigma, MO, USA; 36541, 25 mg/kg) to induce acute vascular senescence. After one week, mice were anesthetized and sacrificed, and then the aorta was collected to detect the degree of endothelial senescence. The mouse model of chronic endothelial senescence in vivo follows the previously described protocol [24, 25]. Briefly, eight-week-old WT and *Sting*$^{-/-}$ mice were subcutaneously injected with an equal amount of saline or D-gal (D-(+)-galactose, Sigma, MO,USA; V900922, 300 mg·kg^{-1}·d^{-1}) for 8 weeks to induce chronic vascular senescence. After 8 weeks of continuous subcutaneous injection, mice were anesthetized and sacrificed, and then the aorta was collected to detect the degree of endothelial senescence.

Atherosclerotic lesion analysis

Apoe$^{-/-}$/AAV9-sh*Sting* and *Apoe*$^{-/-}$/AAV9-shControl male and female mice were fed a Western diet (0.2% cholic acid, 1.2% cholesterol, and 15% fat) for 16 weeks. Mice were then anesthetized, and whole aortas were stained with 2% Oil Red O (Sigma, St. Louis, MO, USA; O0625), and then opened longitudinally and photographed. Additionally, the branciocephalic artery was dissected and embedded in an optimum cutting temperature compound (OCT; BDH Laboratory Supplier) and further cryosectioned into 6-μm-thick sections. The sections were stained with Oil Red O (lesion), hematoxylin and eosin (plaque and necrotic cores), Masson's trichrome (collagen), and CD68 (a macrophage marker) to evaluate the size and morphological composition of atherosclerotic lesions.

ECs senescent models and SA-β-gal staining

Mouse aortic endothelial cells (MAECs) were isolated following a previously described protocol with slight modifications [26, 27]. Briefly, mice were anesthetized, and the aorta was dissected in DMEM and then incubated with diluting type I collagen (Corning, NY, USA; 354236) to a final concentration of 1.75 mg/mL for 36 h after tissue placement. The collagen and aortic were kept hydrated with EGM-2 (Lonza, Switzerland; CC-3156). The explants were cultured at 37 °C and 5% CO_2 in an incubator and monitored every day. Von Willebrand factor (vWF; Proteintech, Wuhan, China; 27186-1-AP) positive staining revealed endothelial cell purity. Human umbilical vein ECs (HUVECs) were isolated from fresh human umbilical veins and cultured in M199 complete medium (Biosharp, Anhui, China; BL309A) as described previously [28]. For replicative senescence, cells of generations 12–18 are considered "senescent", while generations 3–6 are considered "young" controls, as judged by the senescence-associated β-galactosidase (SA-β-gal) assay [29, 30]. ECs were treated with H_2O_2 (100 μM) for 1 h, followed by incubation with Medium 199 for 72 h. A UVB-induced photoaging model was established according to previous studies [31, 32]. Briefly, UVB-irradiation was delivered by a portable narrow-band UVB lamp (Zhongyiboteng, China) emitting at 308–311 nm wavelengths. UVB-irradiation was given a subcytotoxic dose of 10 mJ/cm^2 twice a day for 3 days. At the end of the last stress (0–72 h), cells were collected for further analysis. The irradiation output was monitored using a Waldmann ultraviolet meter (Waldmann, Villigen-Schwenningen, Germany).

SA-β-gal was performed using a senescence detection kit (Beyotime, Shanghai, China; C0602). Briefly, ECs, or aortas, were immersed in freshly prepared SA-β-gal solutions at 37 °C

overnight. Blue staining indicating the presence of SA-β-gal was detected under the microscope.

Mitochondrial function and intracellular redox levels

The detection of intracellular hydrogen peroxide production was established according to previous studies [33, 34]. Briefly, prepare a working solution of 100 μM Amplex-Red reagent (Beyotime, Shanghai, China; ST-010) containing 0.25 U/mL HRP. After H_2O_2 (100 μM, 24 h) or cGAMP (1 μM, 3 h) treatment, 5×10^6 cells were tripsinized and permeabilized with 0.001% digitonin in 4 mL of premixed buffer (65 mM KCl, 2 mM phosphate, 2 mM EGTA, 125 mM sucrose, 10 mM Hepes, 0.2% BSA, and 2 mM $MgCl_2$, pH = 7.2). Begin the reactions by adding 50 μL of the Amplex-Red/HRP solution to each microplate well. Incubate the reactions for 30 min at 37 °C, protected from light. Measure the fluorescence using excitation at 563 nm and emission at 587 nm, respectively. Two different substrate combinations were used: one was a mixture containing 1 mM malate, 1 mM glutamate, 1 mM pyruvate, and 1 mM succinate; the other is 1 mM succinate. At each trace, peroxide release was modulated by adding 1 mM ADP (LEAGENE, China; NP0050), 1.3 μM Oligomycin (Macklin, Shanghai, China; O815255), 10 μM S1QEL (GLPBIO, CA, USA; GC44860), or 1 μM Rotenone (Macklin, Shanghai, China; R817233). Calibration with the hydrogen peroxide standard curve.

ATP content in HUVECs was detected using an assay kit (Beyotime, Shanghai, China; S0062) with luciferase according to the manufacturer's instructions. Briefly, ECs were lysed with ATP buffer, and the supernatant was collected by centrifugation and mixed with luciferase solution to detect chemiluminescence.

For the intracellular superoxide level, living ECs were incubated with 5 μM CM-H2DCF-DA (Invitrogen, Carlsbad, CA, USA; C6827) or 5 μM 2,7-Diamino-10-ethyl-9-phenyl-9,10-dihydrophenanthridine (DHE, Sigma, St. Louis, MO, USA; D7008) according to the manufacturer's instructions.

Mitochondrial membrane potential in ECs was incubated for staining with the JC-1 probe according to the manufacturer's instructions (Beyotime, Shanghai, China; C2006). Malondialdehyde (MDA, S0131S) and superoxide dismutase (SOD, S0101S) activity in ECs suspension and serum in WT or *Sting*$^{-/-}$ mice were measured according to the manufacturer's instructions (Beyotime, Shanghai, China).

Cytosolic dsDNA measurement

Cytosolic DNA was isolated by using a Mitochondria Isolation Kit (Thermo, Waltham, MA, USA; 89801). Briefly, cell suspension was centrifuged at $800 \times g$ for 5 min, and the supernatant was discarded. Reagent ABC was added in order, thoroughly mixed, and incubated for 5 min after each addition. The mixture was centrifuged at $1000 \times g$ for 10 min. The pellet, which contained nuclei, was discarded. The supernatant that contained cytosolic DNA and mitochondria was centrifuged at $12{,}000 \times g$ for 15 min. The supernatant, which contained cytosolic DNA, and the pellet that contained mitochondria were discarded. We then used the DNA Cleanup Kit (NEB, Ipswich, MA, USA; T1030S) to remove residual mitochondrial contamination. The concentration of cytosolic dsDNA was measured using a PicoGreen Kit (Thermo, Waltham, MA, USA; P7589) according to the instructions.

Subcellular fractionation

HUVECs were stimulated with H_2O_2 (100 μM) for 48 h. After treatment, resuspended and incubated in 200 μL digitonin buffer (25 μg/mL Digitonin, 200 mM NaCl, 60 mM HEPES, pH = 7.4) for 15 min. After centrifuging at $3000 \times g$ for 15 min, the supernatants were transferred and centrifuged for 30 min at $15{,}000 \times g$ at 4 °C, and the supernatant was transferred again. Repeat centrifuging three times. The final supernatant is the cytoplasmic part, which is stored for DNA extraction. The initial pellet from the first centrifugation was centrifuged again for 10 min at $15{,}000 \times g$. Pellets were resuspended and incubated in 200 μL NP-40 buffer (1% NP-40, 200 mM NaCl, 60 mM HEPES, pH = 7.4) for 20 min. After 15 min of centrifugation at 8000× *g*, the supernatant contains the mitochondrial portion that is kept for DNA extraction. DNA was then extracted from cytoplasmic and nuclear parts using the QIAmp kit (QIAGEN, Hilden, Germany; 56304).

Cytosolic mtDNA detection

The DNA in the cytosolic fraction was isolated using the QIAmp Kit (QIAGEN, Hilden, Germany; 56304). The mtDNA was detected by RT-PCR using sequences mitochondrially encoded for NADH dehydrogenase 1 (*mt-ND1*), displacement loop region (*D-LOOP*), mitochondrial cytochrome coxidase 2 (*mt-CO2*), and ATP synthase membrane subunit 6 (*mt-ATP6*) as primers. The nuclear DNA was measured by using sequences in the *18S* rDNA (coding 18S ribosomal RNA) as primers. The specific primers were synthesized by Sangon (Shanghai, China), and the primer sequences are shown in Supplementary Table S2.

RNA interference

HUVECs were transfected with 20 nM *STING*-siRNA (5′-GCAUCAAGGAUCGGGUUUA-3′, GenePharma, Suzhou, China) or Control siRNA using RNAiMax (Invitrogen, Carlsbad, CA, USA; 13778-150). The ECs were treated differently within 48 h after siRNA transduction, and then collected for different tests.

Western blotting

Proteins were lysed from cells or tissues using RIPA solution (Beyotime, Shanghai, China; P0013B), and protein concentration was determined using a BCA protein assay kit (Thermo, Waltham, MA, USA). Proteins were separated by electrophoresis and then transferred to polyvinylidene difluoride membranes (Merck Millipore, Germany; HATF00010). After rinsing, the membranes were incubated with the indicated primary antibodies overnight. After incubation with a secondary antibody, chemiluminescence imaging was performed. Antibodies against STING (D2P2F, 13647), p-TBK1 (Ser172, D52C2), p-IRF3 (Ser396, 4D4G), and phospho-Histone H2A.X (Ser139, 2577S) were from Cell Signaling Technology (Danvers, MA, USA); antibodies against STING (19851-1-AP), p53 (60283-2-Ig), p21 (10355-1-AP), NF-κB p65 (80979-1-RR) and Phospho-NF-κB p65 (Ser468, 82335-1-RR) were obtained from Proteintech Group (Wuhan, China); antibodies against ERGIC53 (sc-398777), Calnexin (sc-23954) and Tom20 (FL-145) were from Santa Cruz Biotechnology (Dallas, TX, USA); antibody against dsDNA (ab27156) was purchased from Abcam (Cambridge, UK).

Immunostaining

Aorta sections or ECs were fixed with paraformaldehyde and permeabilized before blocking with fetal goat serum (Boster, Wuhan, China; AR1009) for 45 min. Then it was incubated with primary antibodies overnight. After rinsing, ECs or sections were displayed with a combination of anti-mouse and anti-rabbit antibodies combined with Alexa Fluor 488 or DyLight 594. Images were acquired by auto imaging system (FV 3000, Olympus, Japan).

Immunohistochemistry

For aorta sections, slides were washed with PBS and permeabilized before blocking with an avidin/biotin solution. The sections were incubated with primary antibodies overnight. They were washed in FSGP three times, then incubated with secondary antibodies for 2 h, followed by ABC reagents for 45 min and DAB reagents for 6 min. Images were acquired by auto imaging system (EVOS FL Auto, Life Technologies, Carlsbad, CA, USA).

RT-PCR

Total RNA was extracted using the TRIzol reagent (Takara, Dalian, China; 9108) according to the protocol. Complementary DNA was prepared using the cDNA Synthesis Kit (Thermo, Waltham, MA,

USA; K1622). The RT-PCR was performed using a 2× SYBR-Green Mix (Dongsheng, China; P2091). The data were analyzed using the comparative cycling threshold (ΔΔCt) method. The primers were synthesized by Sangon (Shanghai, China). The primer sequences are shown in Supplementary Table S1.

EdU staining
The proliferation ability of HUVECs was determined using the EdU (5-ethynyl-2′ deoxyuridine) staining kit (RiboBio, Suzhou, China; C00003) according to the protocol. Images were acquired by auto imaging system (EVOS FL Auto, Life Technologies, Carlsbad, CA, USA). The ratio of proliferating cells (red) was normalized to the total cell numbers stained with Hoechst (blue).

In vitro monocyte adhesion assay
THP-1 monocytes in M199 medium were added to HUVECs and incubated for 45 min. Wash with PBS six times to remove unadhered THP-1 cells. The adherent cells were then observed with an inverted microscope. Count the number of THP-1 monocytes that adhere to ECs.

Statistical analysis
The data were represented as the means ± standard error of mean (SEM) from at least three independent experiments in vitro using independent cell cultures or individual animals in vivo. Statistical analyses were performed with GraphPad Prism v8.00. Two-group comparisons were performed with a two-tailed *t* test with or without Welch's correction when the normal distribution was satisfied. One-way ANOVA with Bonferroni *post-hoc* analysis for more than two groups. Statistical significance was accepted at $P < 0.05$ ($^{*}P < 0.05$, $^{**}P < 0.01$, $^{***}P < 0.001$, $^{****}P < 0.0001$).

RESULTS

STING signaling pathway is activated in senescent ECs both in vitro and in vivo
To investigate the relationship between the STING signaling pathway and vascular endothelial senescence, we mined published microarray data (GSE77239) of young and senescent human coronary artery ECs (HCAECs). In addition to up-regulating of cellular senescence and DNA damage pathways, inflammatory pathways (i.e., IFN, TNF, and NF-κB) closely related to STING are also enriched in aging HCAECs, as shown by the enrichment of KEGG signaling pathways (Fig. 1a). Moreover, heat map analysis showed that genes involved in the STING pathway, including *TMEM173, MB21D1, IFN*, and *CXCL10*, were up-regulated in aging HCAECs (Fig. 1b). In order to evaluate the functional role of STING in endothelial senescence, we used different ways to construct endothelial senescence models in human umbilical vein ECs (HUVECs), including oxidative stress senescence caused by H_2O_2, radiation senescence caused by UVB, and replicative senescence caused by cell division and passage characteristics. SA-β-Gal staining was used to evaluate the degree of senescence (Fig. 1c). Remarkably, various aging stimuli caused a robust increase in the protein levels of γ-H2A.X, p21, and p53, the senescence-related indicators, as well as the levels of STING and its phosphorylated forms (p-STING^{S366}) and the phosphorylation levels of TANK binding kinase 1 (TBK1) and interferon regulatory factor 3 (IRF3) downstream of STING (Fig. 1d). Of note, cell replication causes EC senescence and STING activation in a passage-number-dependent manner (Supplementary Fig. S1a), while H_2O_2 induces STING activation in a concentration- and time-dependent manner (Supplementary Fig. S1b, c). Furthermore, in addition to the STING-specific agonist cGAMP, which promoted the entry of p-IRF3^{S396} to the nucleus, H_2O_2, UVB stimulation, or replicating senescence also induced the nuclear translocation of p-IRF3 (Fig. 1e). Similar results were obtained in mouse aortic endothelial cells (MAECs) (Supplementary Fig. S2a, b). Consistent with the in vitro data, in vivo studies revealed that STING expression, dsDNA content, and p-IRF3 levels were significantly increased in the aortic endothelium of mice with paraquat-induced acute vascular aging or D-gal-induced chronic vascular aging (Fig. 1f–i). Collectively, these observations indicate that the STING pathway is significantly upregulated in senescent ECs, both in vitro and in vivo.

STING activation induces, whereas STING knockdown or inhibition alleviates vascular EC inflammation and senescence
We further determine the contribution of STING activation to vascular EC senescence in vitro using both gain- and loss-of-function approaches. To this end, RNA sequencing was performed using the STING-specific agonist cGAMP and the inhibitor H151. As expected, after the regulation of STING by agonists and inhibitors, STING-related pathways, such as the cytosolic DNA-sensing pathway and STING downstream interferon pathways, immune system, DNA damage repair, immune disease, and infectious disease, are all enriched by KEGG (Fig. 2a and Supplementary Fig. S3). In addition, we noticed that cell senescence and SASP-related pathways, such as inflammatory and cytokine pathways (i.e., IFN, TNF, and NF-κB), aging, and cardiovascular disease, are also enriched (Fig. 2a and Supplementary Fig. S3). Notably, the expression levels of genes associated with EC senescence, such as *CDKN1A* (*p21*)*, TP53AIP1, SIRT1*, and *HOMX1*, and genes related to DNA damage repair, such as *MDM2, BCL6, BCL2A1, and C2CD4B*, were substantially upregulated after cGAMP-induced STING activation (Fig. 2b), which were abolished by STING inhibitor H151 (Fig. 2c). Real-time PCR analysis confirmed that cGAMP activation of STING increased the mRNA expression of *p21* and *p16*, as well as the STING downstream inflammatory cytokines *TNFα* and *IFNβ* (Fig. 2d). Moreover, after STING was inhibited by H151, the above inflammatory and aging indicators were significantly reduced. In this study, in addition to regulating STING using cGAMP or H151, small interfering RNA (siRNA) was also used to knock down the transcription and translation levels of STING proteins (Fig. 2e and Supplementary Fig. S4). In accordance with the findings with the STING inhibitor, knockdown of STING by siRNA also inhibited the STING activation-induced mRNA expression of genes involved in inflammation and aging (Fig. 2e). The senescence phenotype showed that both H_2O_2 stimulation and cGAMP activation of STING increased the percentage of SA-β-gal-positive cells, while inhibiting STING with H151 significantly decreased the percentage of senescent HUVECs (Fig. 2f) and MAECs (Supplementary Fig. S2c). In addition, protein levels of both senescence-related indexes, p21 and p53, substantially increased when exposed to H_2O_2 or cGAMP, while H151 effectively reduced H_2O_2-induced expression of p21 and p53 in HUVECs (Fig. 2g) and MAECs (Supplementary Fig. S2d). Accordingly, knockdown of *STING* significantly reduced SA-β-gal activity caused by H_2O_2 stimulation or STING activation (Fig. 2h). Cellular senescence is usually associated with cell cycle arrest [35]. Therefore, EdU probes were used to assist in proving the association between STING and the growth state of senescent ECs. As shown in Fig. 2i, both endothelial senescence caused by H_2O_2 or cGAMP treatment significantly reduced cell proliferation, as evidenced by EdU staining, while *STING* knockdown significantly improved the reduction of proliferation-positive cells. Overall, we adopted various means to confirm that regulation of STING correspondingly regulates EC inflammation and senescence.

CfDNA activates STING to exacerbate EC senescence and mitochondrial dysfunction
Phosphorylated H2AX at Ser139, named γH2A.X, has been widely used as a marker for dsDNA breaks to indicate dsDNA damage [36]. In addition to the chemotherapy drugs Cisplatin and Etoposide, which were used as positive controls for DNA damage, the degree of DNA damage in ECs also increased significantly

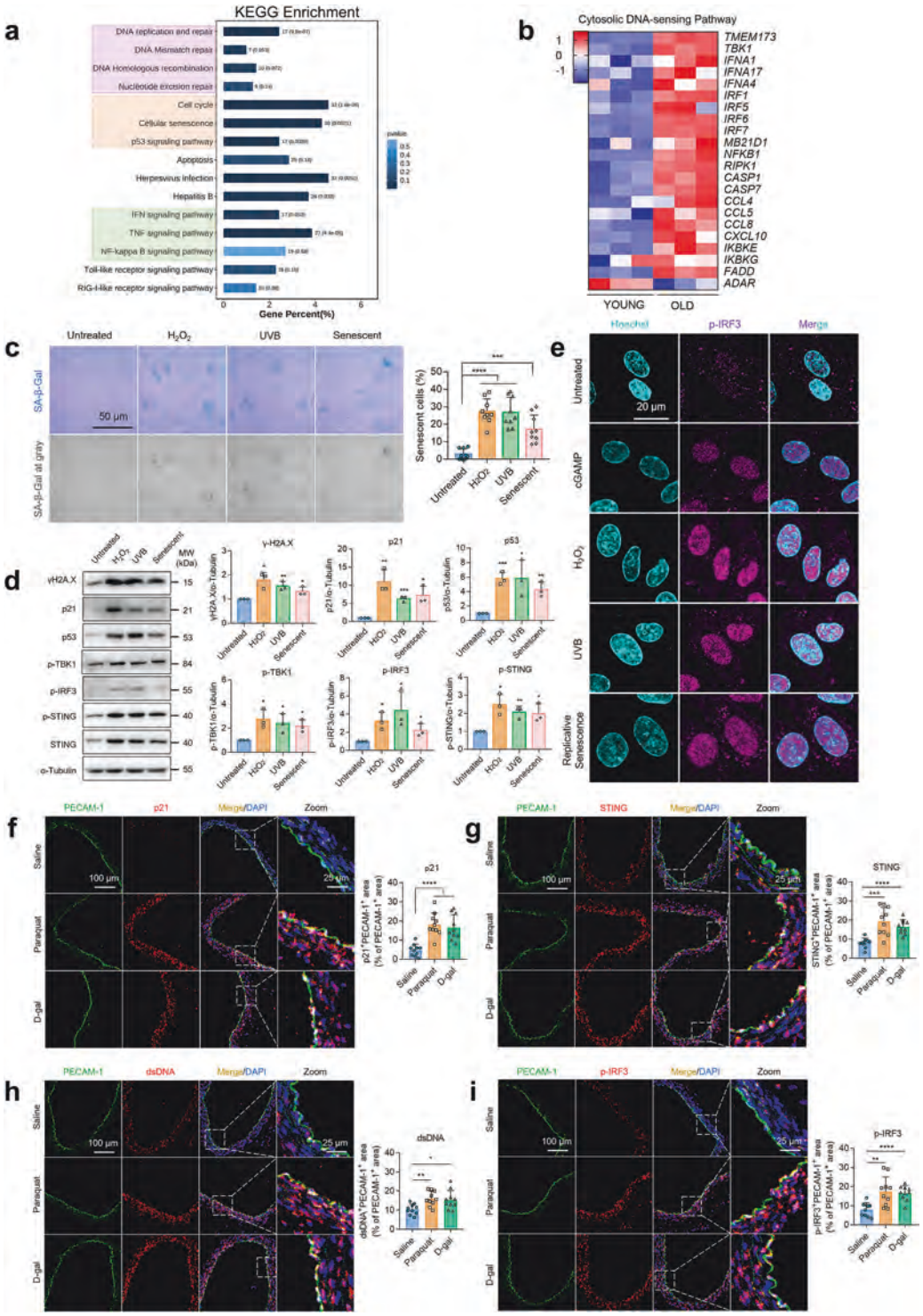

Fig. 1 Upregulation of the STING signaling pathway in various aging models, both in vitro and in vivo. a KEGG pathway enrichment map showing pathway enrichment in young and aging HCAECs by analysis of GEO datasets (GSE77239). **b** Heat map showing the gene expression profile of both young and aged HCAECs by analysis of GSE77239. **c** SA-β-gal staining of premature senescent HUVECs at third generations treated with H_2O_2 (100 μM, 72 h) or UVB radiation (10 mJ/cm^2, 72 h) and replicative senescent HUVECs at 18th generations. Scale bar: 50 μm. The quantification of the senescence cell ratio is shown in the right panel. $n = 9$ per group. **d** Immunoblot analysis of the protein expression of senescence-related indicators (γ-H2A.X, p21, p53) and STING pathway-related indicators (p-TBK1, p-IRF3, p-STING, STING) in the third generation of HUVECs treated with H_2O_2 (100 μM, 72 h) or UVB radiation (10 mJ/cm^2, 72 h) and in the 18th generation of HUVECs. The relative protein expression level is shown in the right panel. $n = 3$ per group. **e** Immunofluorescent staining of p-IRF3 was performed in the third generation of HUVECs treated with cGAMP (500 nM, 12 h) or H_2O_2 or UVB radiation, and in the 18th generation of HUVECs (replicative senescence). Eight-week-old WT C57BL/6J mice were single intraperitoneally injected with equal amounts of paraquat (25 mg/kg) to induce acute vascular senescence. In addition, 8-week-old WT mice were daily subcutaneously injected with an equal amount of D-gal (300 mg·kg^{-1}·d^{-1}) for continuous treatment for 8 weeks to induce chronic vascular senescence. Immunofluorescent staining of p21 (**f**), STING (**g**), dsDNA (**h**), and p-IRF3 (**i**) in the frozen aortic sections of mice treated with saline, paraquat (25 mg/kg) and D-gal (300 mg·kg^{-1}·d^{-1}). PECAM-1 positive area indicates the endothelial layer. DAPI indicates the cell nucleus of the vasculature. $n = 10$ per group. Data were presented as means ± SEM; $^{*}P < 0.05$, $^{**}P < 0.01$, $^{***}P < 0.001$, $^{****}P < 0.0001$ was considered significant.

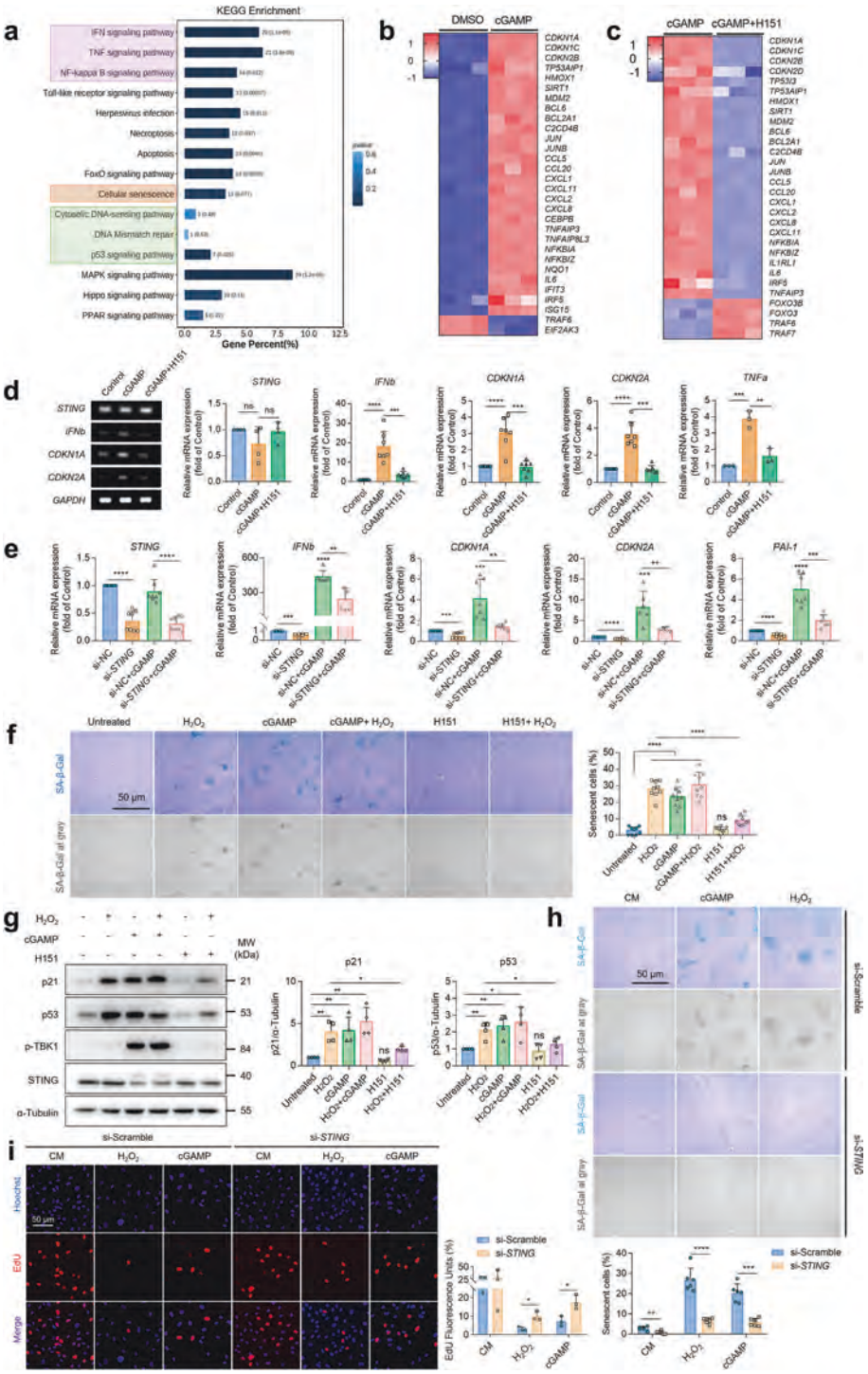

Fig. 2 Intervention with STING through knockdowns or inhibitors significantly alleviates EC inflammation and senescence. a KEGG pathway enrichment of cGAMP-treated HUVECs revealed by RNA sequencing analysis. Differential genes of cGAMP-treated HUVECs (**b**) or cGAMP plus H151-treated HUVECs (**c**) were revealed by transcriptomic profiling. **d** RT-PCR analysis of mRNA levels of *STING, IFNb, CDKN1A* (*p21*), *CDKN2A* (*p16*), and *TNFa* in HUVECs treated with 500 nM of cGAMP for 12 h in the presence or absence of STING-specific inhibitor H151 (10 μM, 12 h). The data are normalized to *GAPDH* mRNA transcript levels. **e** Real-time PCR was performed to measure the mRNA levels of *STING, IFNb, CDKN1A, CDKN2A*, and *PAI-1* in HUVECs transfected with 100 nM of *STING* siRNA or a nontargeted siRNA control (si-Scramble) for 48 h in the presence or absence of cGAMP (500 nM, 6 h). **f** SA-β-gal staining of HUVECs treated with or without H_2O_2 in the presence or absence of cGAMP or H151. Scale bar: 50 μm. The quantification of the senescence cell ratio is shown in the right panel ($n = 9$ per group). **g** Immunoblot analysis of the protein expression of p21 and p53 in HUVECs treated as in (**f**). The quantification of protein levels is shown in the right panel. SA-β-gal staining showing the ratio of senescence HUVECs ($n = 9$ per group) (**h**); and EdU staining showing the ratio of proliferating HUVECs ($n = 3$ per group) (**i**) treated with 100 nM of *STING* siRNA or si-Scramble, in the presence or absence of H_2O_2 or cGAMP. Scale bar: 50 μm. Data were presented as means ± SEM from at least three independent experiments. $^{*}P < 0.05$, $^{**}P < 0.01$, $^{***}P < 0.001$, $^{****}P < 0.0001$ was considered significant; ns, not significant.

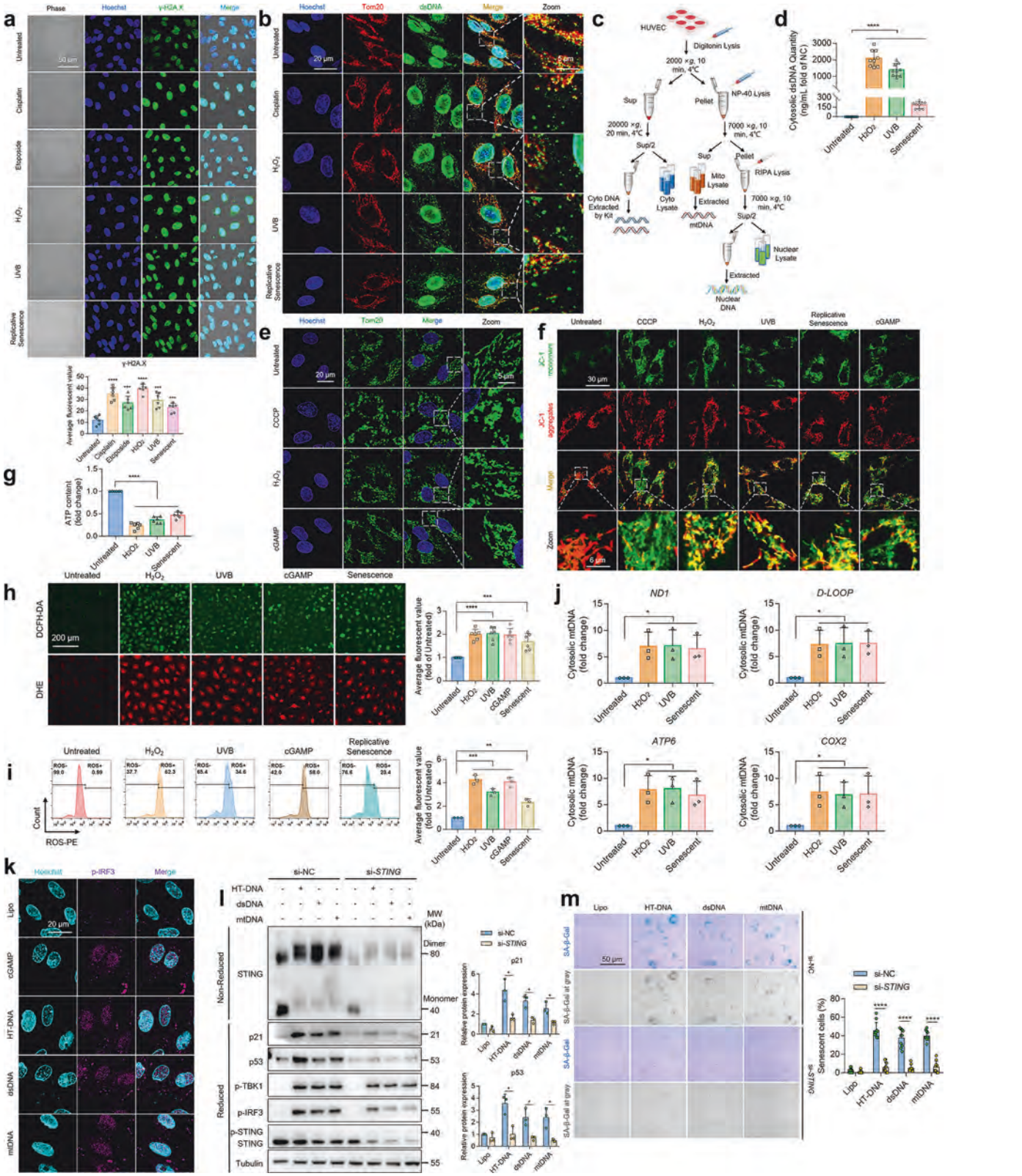

under various aging models caused by H_2O_2, UVB, and division replication (Fig. 3a). Using dsDNA antibodies labeled with intracellular dsDNA, H_2O_2 and UVB-stimulated cells or replicated senescent cells substantially increased the amount of cfDNA (Fig. 3b). In addition to the qualitative experiments represented by immunofluorescence, we continued to obtain cytoplasmic components by removing nuclei, mitochondria, and other organelles through organelle separation, and extracted and quantified cfDNA to establish quantitative analysis (Fig. 3c, d), which further confirmed that EC senescence would cause nuclear DNA damage

Fig. 3 dsDNA and mtDNA are the true triggers that activate STING and lead to endothelial senescence. a The expression level of γ-H2A.X was detected by fluorescence brightness in HUVECs treated with H_2O_2 or UVB radiation and in replicative senescent ECs. Cisplatin (10 μM, 6 h) and Etoposide (10 μM, 6 h) as positive controls for DNA damage in HUVECs. The average fluorescence value is shown in the bottom panel. **b** The degree of cytoplasmic dsDNA release was detected by immunofluorescence imaging in HUVECs treated as described in a. The HUVECs were stained with anti-dsDNA antibodies (green) and anti-Tom20 antibodies (red) and further visualized by confocal microscopy. Cisplatin (10 μM, 6 h) as a DNA damage inducer serves as a positive control for dsDNA release. **c** Schematic of cell lysis and centrifugation for subcellular fractionation. **d** A bar graph showing that the quantity of cytosolic dsDNA was increased in aging HUVECs caused by different methods (H_2O_2 stimulation, UVB radiation, and replicative senescence) compared with young untreated HUVECs ($n = 9$ per group). **e** The HUVECs were treated with or without CCCP (20 μM, 6 h) or H_2O_2 or cGAMP (500 nM, 6 h) and then stained with mitochondrial indicator antibody (Tom20), and images were then captured by confocal microscopy. CCCP, as a mitochondrial uncoupling agent, serves as a positive control for mitochondrial morphological changes. Scale bar: 20 μm. **f** Mitochondrial membrane potential was detected by JC-1 staining and captured by confocal microscopy in HUVECs treated as described in (**a**) and (**e**). **g** ATP content was measured by a luminometer in young and aged HUVEC cells caused by different methods (H_2O_2 stimulation, UVB radiation, and replicative senescence). Detection of ROS levels indicated by DCFH-DA and DHE probes using fluorescence imaging (**h**) and flow cytometry (**i**) was performed in HUVECs treated as described in (**f**). ROS's average fluorescence value is shown in the right panel. **j** Detection of free mtDNA content in the cytoplasm. Total DNA was harvested from the cytosolic and nuclear fractions of various senescent HUVECs and analyzed by RT-PCR. Cytosolic *mtDNA* genes were normalized to respective 18S and presented as fold enrichment over media-treated controls. **k** Immunofluorescent staining of p-IRF3 was performed in HUVECs treated with cGAMP (500 nM, 6 h) or transfected with 1 μg/mL extracellular DNA (HTDNA, dsDNA, or mtDNA) for 6 h. cGAMP and HTDNA, as STING agonists, serve as positive controls for the p-IRF3 nucleation phenomenon here. Immunoblot analysis (**l**) of senescence indicators and STING pathway-related indicator protein levels in HUVECs that were transfected with 100 nM of *STING* siRNA or nontargeted siRNA control (si-NC) for 48 h in the presence or absence of extracellular DNA transfected for 6 h at a final concentration of 1 μg/mL. Meanwhile, non-reducing electrophoresis was used to indicate the degree of dimerization of STING. SA-β-gal staining (**m**) was performed in HUVECs treated as in (**l**). Scale bar: 50 μm. The quantification of the senescence cell ratio is shown in the right panel. Data were presented as means ± SEM from at least three independent experiments. $^{*}P < 0.05$, $^{**}P < 0.01$, $^{***}P < 0.001$, $^{****}P < 0.0001$ was considered significant.

and proved that the damaged DNA would be released into the cytoplasm in a free state. In addition to the nucleus, we posited that the cfDNA released from senescent ECs also originates from damaged mitochondria under aging stress. To test this hypothesis, we investigated mitochondrial morphology and function under various aging stimuli. Firstly, we found that, in addition to the CCCP, a mitochondrial coupling agent used here as a positive control of mitochondrial morphology changes, cGAMP or H_2O_2 stimulation also caused an abnormal mitochondrial morphological change (Fig. 3e). Secondly, JC-1 staining revealed that the mitochondrial membrane potential of ECs was markedly decreased by diverse aging stimuli and cGAMP treatment (Fig. 3f). Thirdly, the content of mitochondrial ATP production in ECs decreased markedly under the above various aging models (Fig. 3g). We further detected the ROS levels using two kinds of ROS probes, DCFH-DA and DHE. Both fluorescence imaging and FACS experiments showed that mROS levels in ECs increased significantly under various senescent models or STING activation conditions (Fig. 3h, i). In addition, the hydrogen peroxide generation experiment also proved that the intracellular hydrogen peroxide level was increased under H_2O_2 or cGAMP treatment (Supplementary Fig. S5a). The cellular content of SOD and MDA reflected the antioxidant capacity of ECs. As shown in Supplementary Fig. S5b–d, the lysate of ECs treated with H_2O_2 or cGAMP showed a decreased SOD level and increased MDA content. Finally, the contents of mitochondria-specific coding genes *ND1*, *D-LOOP*, *ATP6*, and *COX2* were then determined. Cytoplasmic components without nuclei and mitochondria are further obtained by organelle isolation, and cfDNA is extracted as a reaction template for qPCR. The results showed that the mitochondria of ECs were damaged and mtDNA was released into the cytoplasm under ECs senescence (Fig. 3c, j). Taken all together, these results indicate that various aging stimuli and STING activation-induced EC senescence causes nuclear DNA damage and mitochondrial dysfunction, thereby promoting the release of dsDNA and mtDNA into the cytoplasm.

We next tested whether the release of free dsDNA and mtDNA into the cytoplasm is the real promoter of STING activation and EC senescence. Therefore, we continued to obtain dsDNA and mtDNA through organelle isolation and then transfected them into cells through transfection to detect STING activation level and senescence degree. The degree of nuclear translocation of p-IRF3 indicates the activation of the STING pathway. As shown in Fig. 3k, transfection with HT-DNA, dsDNA, and mtDNA, as well as a treatment with the STING agonist cGAMP, resulted in the obvious nuclear translocation of p-IRF3 in ECs. In addition, the degree of STING dimerization and the levels of p-TBK1, p-IRF3, and p-STING, as well as senescence-related markers, were all increased in ECs transfected with HT-DNA, dsDNA, or mtDNA. Interestingly, all of the above indexes were largely attenuated when *STING* was knocked down by siRNA (Fig. 3l). Furthermore, the percentage of SA-β-Gal staining positive cells was remarkably increased after transfection with HT-DNA, ds-DNA, or mt-DNA, while after *STING* knockdown abrogated the effect of dsDNA on SA-β-Gal activity (Fig. 3m). Therefore, these findings indicate that under aging pressure, the nucleus and mitochondria in ECs were damaged, and cfDNA was released to the cytoplasm, leading to STING activation as the real culprit of EC senescence.

Age-related endothelial inflammation is exacerbated by STING activating the SASP process within the senescent microenvironment

Certain SASP factors, such as interferon and inflammatory factors, as the critical inflammatory mediators of the STING pathway, participate in the innate immune response, and IRF3 and NF-κB closely regulate the production of interferon and inflammatory factors, respectively [37]. To explore the link between STING and SASP in vascular endothelial senescence, we first tested whether STING regulates the activation of NF-κB. We found that NF-κB signaling was activated in various models of EC aging, as indicated by the nucleation of NF-κB p65 (Fig. 4a) and the phosphorylated NF-κB p65 Ser536 modification (Fig. 4b). In addition to Etoposide as a positive agonist of NF-κB, which significantly promoted the nucleation of p65 [38], recombinant proteins of TNFα and IFNβ, as crucial members of the downstream inflammatory pathways of STING, robustly induced the nucleation of p65 to exert inflammatory effects (Fig. 4c). To further investigate whether the inflammatory factors released by STING activation aggravate endothelial senescence, we performed SA-β-gal staining and found that SA-β-gal-positive cells increased significantly after TNFα and IFNβ treatment (Fig. 4d). In addition to H_2O_2, TNFα and IFNβ also increased p21 and p53 protein levels, as revealed by Western blotting (Fig. 4e). HT-DNA, as the upstream stimulating molecule of STING, induced the entry of p65 into the nucleus, which was completely abrogated by STING knockdown (Fig. 4f). In contrast, STING knockdown did not affect NF-κB p65 nuclear translocation induced by TNFα and IFNβ, the downstream

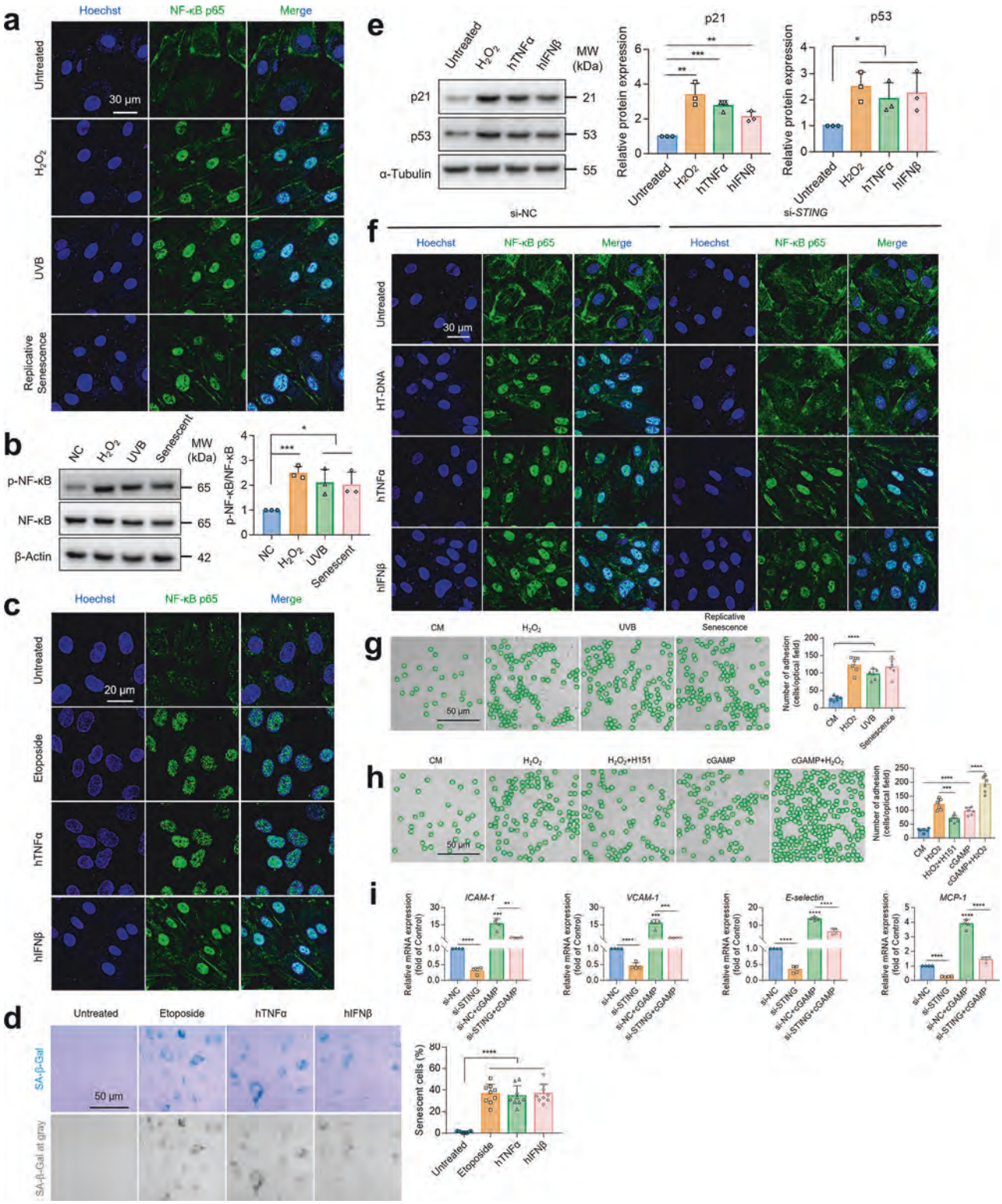

inflammatory molecules of STING (Fig. 4f). Because monocyte adhesion to vascular endothelium is an essential inflammatory event in vascular aging-related CVDs, we conducted monocyte adhesion experiments by HUVECs and THP-1 co-culture, which showed that the number of firmly adhering human monocytes to senescent ECs caused by various means increased substantially compared with the control group (Fig. 4g). Moreover, in addition to H_2O_2 stimulation, cGAMP-induced STING activation also markedly induced monocyte adhesion. Importantly, cGAMP treatment exacerbated the effect of H_2O_2-mediated monocyte adhesion, while inhibiting STING with H151 markedly decreased the H_2O_2-mediated effect on monocyte adhesion (Fig. 4h). Finally, STING knockdown significantly downregulated cGAMP-induced mRNA expression of inflammatory adhesion factors (*VCAM-1*,

Fig. 4 Age-related endothelial inflammation is exacerbated by STING activating the SASP process within the senescent microenvironment. a The nuclear translocation of NF-κB p65 was detected by immunofluorescent staining of NF-κB p65 in HUVECs treated with or without H_2O_2 or UVB radiation and in replicative senescent ECs. Scale bar: 30 μm. **b** Immunoblot analysis of p-NF-κB protein levels in HUVECs treated as in (**a**). Quantification of p-NF-κB levels is shown in the right panel. **c** Immunofluorescent staining of NF-κB p65 in HUVECs treated with Etoposide (10 μM) or hTNFα (50 ng/mL) or hIFNβ (50 ng/mL) stimulation for 6 h. Scale bar: 20 μm. **d** SA-β-gal staining was performed in HUVECs treated with or without Etoposide (10 μM) or hTNFα (50 ng/mL) or hIFNβ (50 ng/mL) stimulation for 24 h. Scale bar: 50 μm. The quantification of senescent cell ratio is shown in the right panel. **e** Immunoblot analysis of p53 and p21 protein levels in HUVECs stimulated with or without H_2O_2, hTNFα, or hIFNβ. Quantification of p53 and p21 levels is shown in the right panel. **f** Immunofluorescent staining of NF-κB p65 in HUVECs treated with 100 nM of *STING* siRNA (si*STING*) or nontargeted siRNA control (si-NC), in the presence or absence of extracellular DNA (HT-DNA) transfected at a final concentration of 1 μg/mL or recombinant inflammatory factors (hTNFα, hIFNβ) treated at a final concentration of 50 ng/mL for 6 h. Scale bar: 30 μm. **g** The monocyte adhesion assay was performed in HUVECs treated with H_2O_2 or UVB radiation and in replicative senescent ECs. The number of adherent cells is shown in the right panel. **h** The monocyte adhesion assay was performed in HUVECs treated with or without H_2O_2 in the presence or absence of cGAMP (500 nM, 12 h) or H151 (10 μM, 12 h). Scale bar: 50 μm. **i** RT-PCR was performed to measure the mRNA levels of *ICAM-1, VCAM-1, E-selectin*, and *MCP-1* in HUVECs transfected with si*STING* or si-NC in the presence or absence of cGAMP (500 nM, 12 h). Data were presented as means ± SEM from at least three independent experiments. $^{*}P < 0.05$, $^{**}P < 0.01$, $^{***}P < 0.001$, $^{****}P < 0.0001$ was considered significant; ns not significant.

ICAM-1, E-selectin, and *MCP-1*) (Fig. 4i). Collectively, these observations demonstrate that STING induces downstream NF-κB and IRF3 activation, thereby producing various SASP factors (e.g, TNFα, IFNβ, and cfDNA) to further aggravate vascular endothelial inflammation and senescence.

EC-specific *Sting* knockdown retards vascular endothelial inflammation and senescence

To further verify the essential role of STING in vascular endothelial senescence in vivo, we generated endothelial-specific *Sting*-knockdown mice (AAV9-sh*Sting*) using an adeno-associated viral vector (AAV9-ICAM2-GFP-RGDLRVS). C57BL/6J mice were injected with AAV9-sh*Sting* or the control virus (AAV9-shControl) for two weeks to induce *Sting* knockdown, followed by treatment with paraquat, a herbicide that is able to induce vascular senescence in mice [22] (Fig. 5a). Fluorescence imaging of tissue organs showed that the AAV9 virus specifically infected the aorta and that AAV9-GFP was specifically expressed in the aortic vessels (Fig. 5b). Immunofluorescence staining showed that STING expression was markedly reduced in the aortic endothelium of mice receiving AAV9-sh*Sting* (Fig. 5d), confirming the effective and specific deletion of STING in vascular ECs. Importantly, EC-specific *Sting* deficiency mitigated paraquat-induced vascular senescence in vivo, as indicated by SA-β-gal staining (Fig. 5c). Accordingly, compared with the control group, expression of p21 and p53, the indicators of acute vascular aging caused by Paraquat, was markedly decreased in the aortic ECs of endothelial-specific *Sting*-knockdown mice (Fig. 5e, f). Interestingly, with the knockdown of *Sting* in vascular ECs, the dsDNA content level and DNA damage index γ-H2A.X in the aortic endothelial region were correspondingly reduced (Fig. 5g, h). In addition, we found that the p-IRF3 and p-NF-κB-positive areas in the endothelial tissue were significantly reduced after endothelial-specific *Sting* knockdown (Fig. 5i, j), implying that *Sting* deletion in vascular ECs might be capable of blocking downstream IFN and inflammatory pathways in vivo.

Global *Sting* deficiency attenuates paraquat-induced acute vascular aging and D-gal-induced chronic vascular aging in mice

To evaluate STING as a potential therapeutic target, we further investigated the effect of global *Sting* deficiency on vascular aging. Global *Sting* knockout mice ($Sting^{-/-}$) and the littermate controls ($Sting^{+/+}$, WT) were treated with paraquat to establish an acute aging model in vivo (Fig. 6a). *Sting* knockout efficiency was verified by protein immunoblotting, qPCR, and vascular section staining of STING in aortas from WT and $Sting^{-/-}$ mice (Fig. 6b, c, and Supplementary Fig. S6a–e). There was no difference in lipid levels between groups (Supplementary Fig. S7). As shown in Fig. 6d, global *Sting* knockout decreased aortic ROS production compared with WT mice. In addition, the levels of MDA and SOD in serum indicate that global $Sting^{-/-}$ can effectively alleviate the damage of lipid oxidation (Supplementary Fig. S5d, e). Moreover, SA-β-gal staining of the aortic endothelium showed that acute endothelial senescence induced by paraquat was largely alleviated in *Sting*-deficient mice compared with WT mice (Fig. 6e). Additionally, the expression of aging and DNA damage-related indicators p21, p53, γ-H2A.X, and dsDNA, as well as STING downstream inflammatory indicators such as p-IRF3 and p-NF-κB, were all markedly reduced in the vascular ECs of $Sting^{-/-}$ mice (Fig. 6g–l).

To further verify the role of STING in vascular endothelial aging in vivo, chronic vascular aging was also established by a daily subcutaneous injection of D-gal and continuous treatment for 8 weeks (Fig. 7a, b). DHE staining showed that ROS production in the aorta was markedly reduced in $Sting^{-/-}$ mice (Fig. 7c). The degree of lipid oxidative damage was also mitigated by the detection of MDA and SOD in the serum of $Sting^{-/-}$ mice (Supplementary Fig. S5f, g). Notably, SA-β-gal staining revealed that *Sting* deficiency mitigated D-gal-induced chronic vascular senescence in vivo (Fig. 7d). Furthermore, we observed decreased senescence-related indexes such as p21 and p53 (Fig. 7f, g), DNA damage-related indexes such as γ-H2A.X and dsDNA (Fig. 7h, i), as well as inflammatory mediators associated with the STING pathway such as p-IRF and p-NF-κB in the aortic endothelium of D-gal-treated $Sting^{-/-}$ mice (Fig. 7j, k).

Collectively, these findings indicate that global *Sting* deficiency could alleviate both paraquat-induced acute vascular aging and D-gal-induced chronic vascular aging in mice via inhibition of the dsDNA-STING-IRF3/NF-κB axis.

Identification of Cilostazol as a novel STING inhibitor that mitigates vascular endothelial inflammation and senescence

Have shown that STING plays a critical role in vascular endothelial senescence both in vitro and in vivo. We next asked whether a certain clinical drug with known vasoprotective effects could inhibit the STING pathway and vascular aging. We performed in-house compound screening of 10 selected FDA-approved vasoprotective drugs, and the results showed that, compared with H151, a potent antagonist of STING [39], Cilostazol also significantly inhibited the phosphorylation of STING, TBK1, and IRF3 caused by STING activation by cGAMP, or SR717, a non-nucleotide STING agonist [40] (Fig. 8a, b). Moreover, the dose-effect experiment further confirmed that Cilostazol inhibited the STING pathway in a dose-dependent manner, as evidenced by reduced phosphorylation levels of TBK1 and IRF3 in both HUVECs (Fig. 8c) and MAECs (Supplementary Fig. S8a) and decreased mRNA levels of STING-related inflammatory mediators such as *IFNβ, TNFα*, and *CXCL10* (Fig. 8d). Furthermore, functional experiments showed that Cilostazol suppressed STING activation-induced endothelial senescence in a dose-dependent

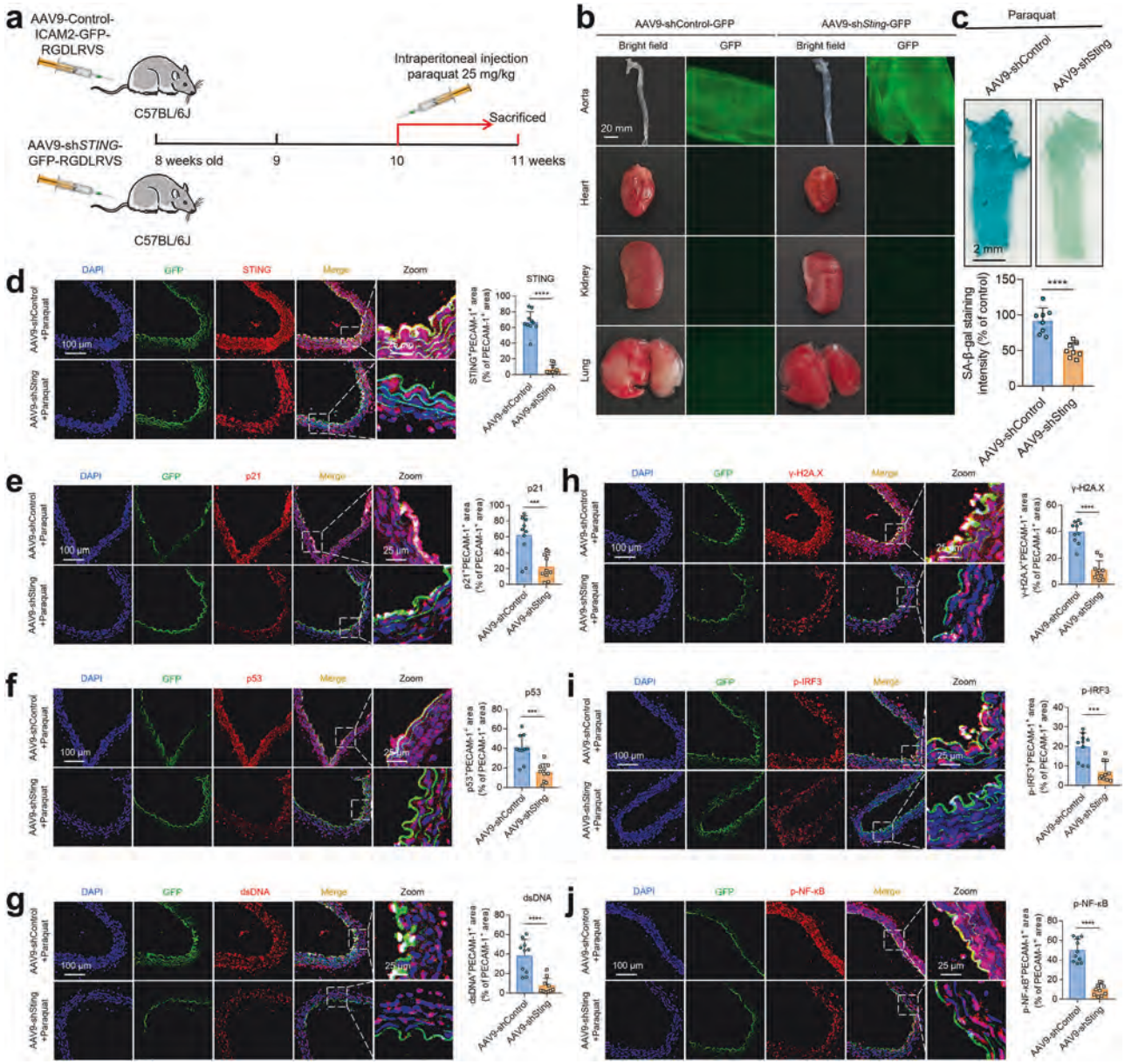

Fig. 5 EC-specific *Sting* deficiency significantly alleviates vascular endothelial aging. a Schematic diagram of the animal experimental process. C57BL/6J mice were injected with AAV containing the sh*Sting* coding sequence and GFP protein (AAV9-ICAM2-sh*Sting*-GFP-RGDLRVS) or control viruses only containing GFP protein (AAV9-ICAM2-GFP-RGDLRVS) using 5×10^{11} vector genomes (vg)/mouse. After virus expression for 2 weeks and a single intraperitoneal injection of an equal amount of paraquat (25 mg/kg), the aorta was isolated from the mice, and the degree of endothelial senescence was detected. **b** Mouse organs in each group were extracted for fluorescence imaging. Both bright field and GFP fluorescence signals were captured at the same capture conditions. Scale bar: 20 mm. **c** SA-β-gal staining of the inner layer of aortas of EC-specific *Sting*-deficient mice and controls ($n = 8$ per group). **d** Immunofluorescent staining of STING in the frozen aortic sections of mice to evaluate the knockdown efficiency of *Sting* in vascular ECs. PECAM-1 indicates the endothelial layer. DAPI indicates the cell nucleus. Scale bar: 100 μm. The percentages of $STING^+PECAM\text{-}1^+$ area to $PECAM\text{-}1^+$ area were calculated ($n = 10$ mice per group). Representative images of immunostaining for p21 (**e**), p53 (**f**), dsDNA (**g**), γ-H2A.X (**h**), p-IRF3 (**i**), and p-NF-κB p65 (**j**). Scale bar: 100 μm. Data were presented as means ± SEM. $^{**}P < 0.01$, $^{***}P < 0.001$, $^{****}P < 0.0001$ was considered significant.

manner, as indicated by reduced mRNA levels of *p21, p16*, and *PAI-1* (Fig. 8e), downregulated protein expression of p21 and p53 induced by HT-DNA (Fig. 8f), and decreased SA-β-gal-positive senescent cells (Fig. 8g and Supplementary Fig. S8b). Subsequently, using virtual docking, we found that Cilostazol successfully docked with STING at S162 and S243 sites (Fig. 8h, i), which had been described in previous studies as being involved in STING activation [41–46]. After activation, STING will translocate from the endoplasmic reticulum (ER) to the endoplasmic reticulum-Golgi intermediate compartment (ERGIC) and then to the Golgi apparatus, where it recruits and phosphorylates downstream TBK1 and IRF3 [47, 48]. Interestingly, using Calnexin, ERGIC53, and TGN46 to label ER, ERGIC, and Golgi, respectively, we observed that Cilostazol hindered STING translocation from ER to Golgi apparatus during cGAMP treatment (Fig. 8j, k). Surprisingly, the inhibitory effect of Cilostazol on STING's translocation from ER to Golgi was largely abrogated when STING's S162 and S243 sites were mutated (Supplementary Fig. S9), suggesting that Cilostazol inhibits STING translocation from ER to Golgi apparatus during STING activation by targeting its S162 and S243 sites.

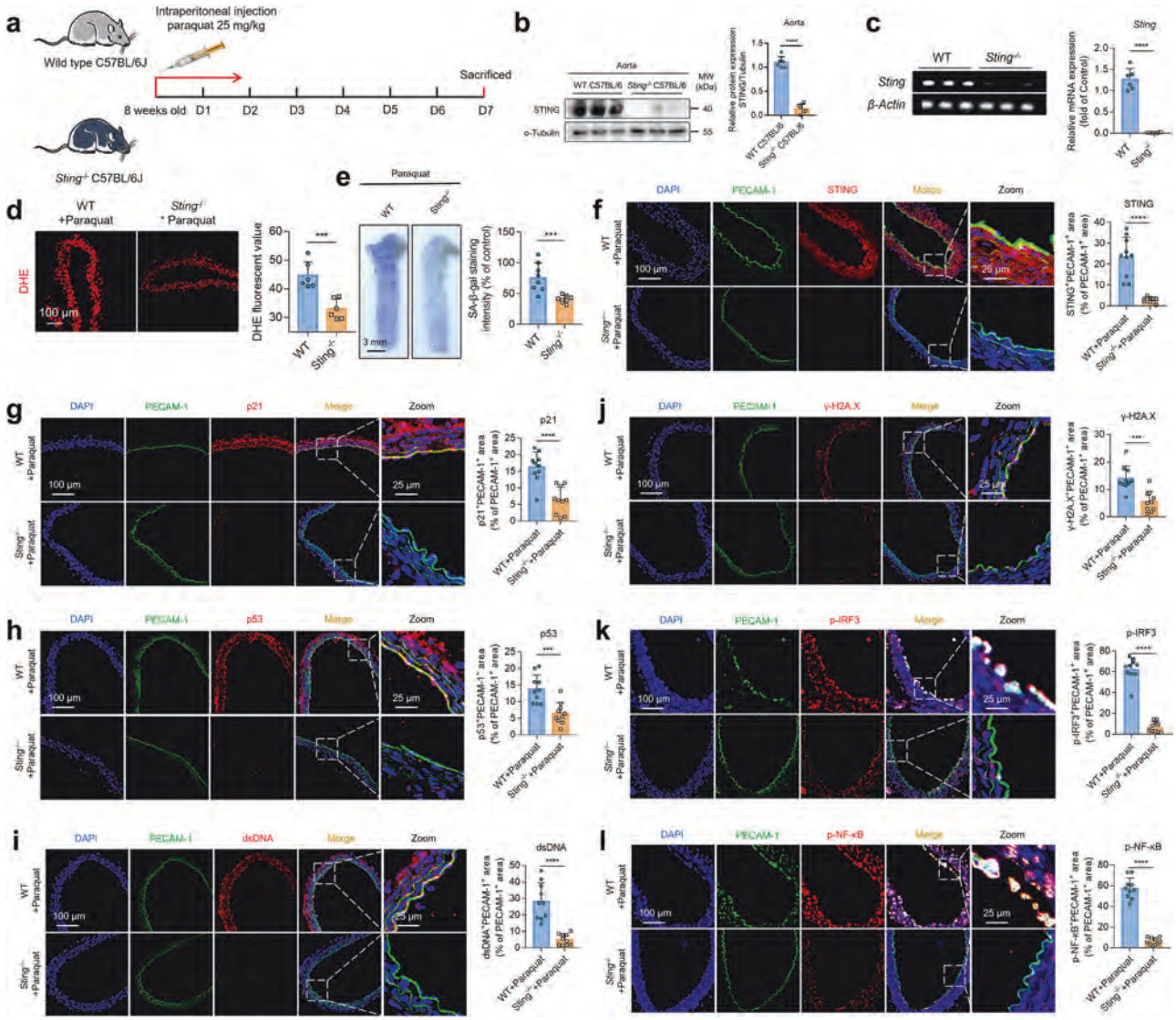

Fig. 6 Significant improvement in paraquat-induced acute vascular inflammation and senescence in *Sting*$^{-/-}$ mice. a Schematic diagram of the animal experimental process. Eight-week-old WT and *Sting*$^{-/-}$ mice were single intraperitoneally injected with equal amounts of paraquat (25 mg/kg) to induce acute vascular senescence. Western blotting (**b**) and RT-PCR (**c**) were performed from both protein and RNA perspectives to evaluate the knockout efficiency of *Sting* in mouse aortae. **d** DHE staining of the frozen aortic sections to detect ROS levels. **e** SA-β-gal staining of the inner layer of aortas of WT and *Sting*$^{-/-}$ mice ($n = 8$ mice per group). **f** Immunofluorescent staining of STING in the frozen aortic sections of mice. PECAM-1 indicates the endothelial layer. DAPI indicates the cell nucleus. Scale bar: 100 μm. The percentages of STING^{+}PECAM-1^{+} area to PECAM-1^{+} area were calculated ($n = 10$ mice per group). Representative images of immunostaining for p21 (**g**), p53 (**h**), dsDNA (**i**), γ-H2A.X (**j**), p-IRF3 (**k**), and p-NF-κB p65 (**l**) in the aortic endothelium of WT and *Sting*$^{-/-}$ mice. Scale bar: 100 μm. Data were presented as means ± SEM. ***$P < 0.001$, ****$P < 0.0001$ was considered significant.

We further evaluated the effects of Cilostazol and the known STING inhibitor C-176 on vascular endothelial senescence in vivo (Supplementary Fig. S10a). The SA-β-gal staining of the vascular endothelium showed that C-176 or Cilostazol treatment significantly prevented vascular endothelial senescence in paraquat-induced vascular senescence in mice (Supplementary Fig. S10b). Moreover, ROS production (Supplementary Fig. S10c), positive areas of STING (Supplementary Fig. S10d), aging indicators p21 and p53 (Supplementary Fig. S10e, f), DNA damage indicators such as γ-H2A.X and dsDNA (Supplementary Fig. S10g, h), as well as STING downstream IFN and inflammatory mediators p-IRF3 and p-NF-κB (Supplementary Fig. S10i, j) in the aortic endothelium, were all significantly reduced by Cilostazol or C-176 treatment. Together, these findings indicate that inhibiting STING could be an effective intervention strategy for vascular endothelial senescence.

EC-specific *Sting* knockdown reduced EC inflammation, mitochondrial dysfunction, and the development of atherosclerosis in *Apoe*$^{-/-}$ mice

To further determine whether endothelial STING contributes to the formation of atherosclerotic lesions through promoting aging-related endothelial inflammation and mitochondrial dysfunction, *Apoe*$^{-/-}$/AAV9-sh*Sting* mice and *Apoe*$^{-/-}$/AAV9-shControl mice were fed a Western diet for 16 weeks (Fig. 9a). Oil Red O staining revealed significantly decreased lesion sizes in the whole aorta and aortic arch of *Apoe*$^{-/-}$/AAV9-sh*Sting* mice in comparison with *Apoe*$^{-/-}$/AAV9-shControl (Fig. 9b, c). To evaluate the effect of EC-specific *Sting* deletion on the morphological composition of atherosclerotic plaques, H&E, Masson trichromatic, and immunohistochemical staining were performed on the cross-sections of the aorta brachiocephalic trunk. Remarkably, the necrotic core areas and the amount of macrophages in

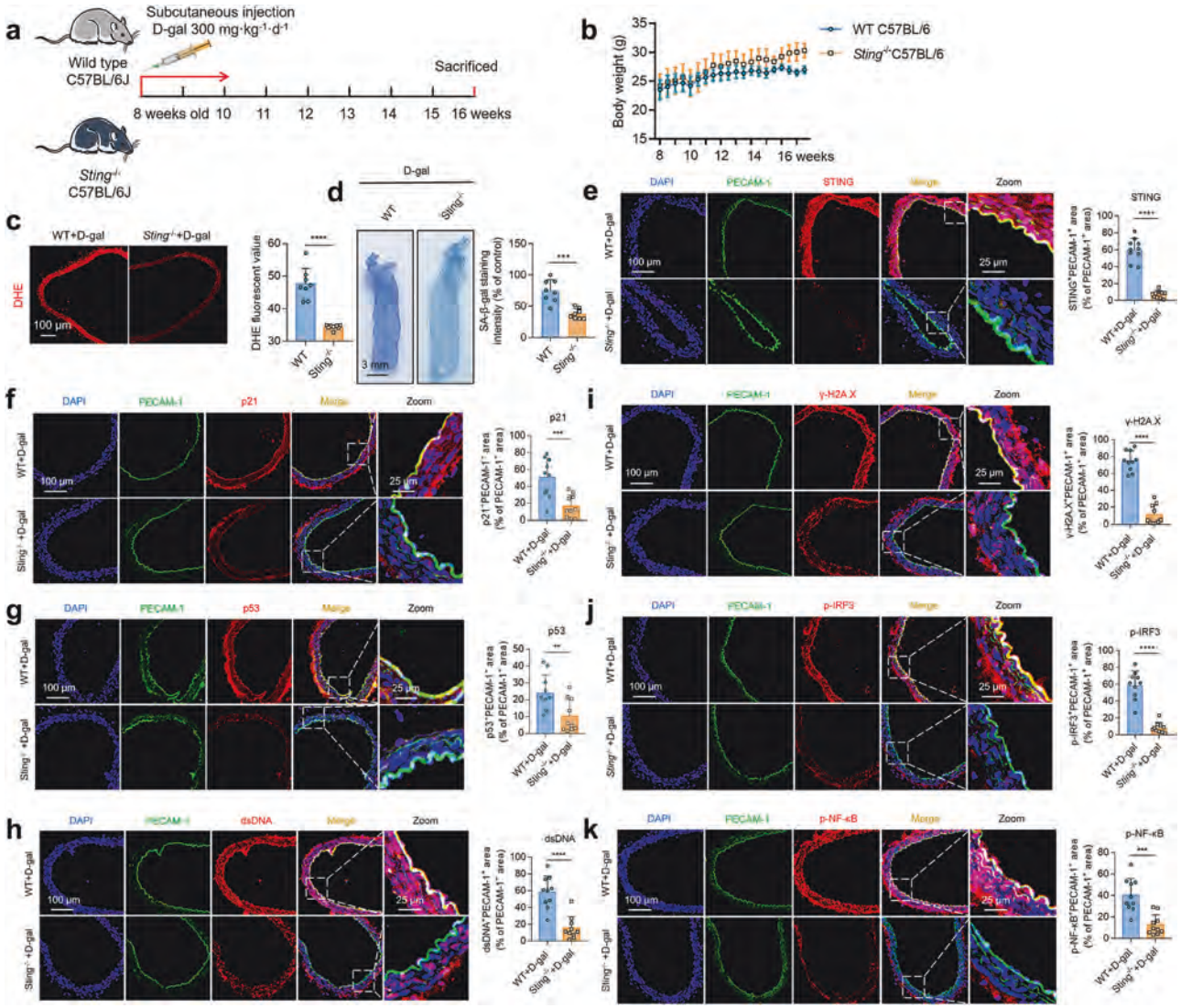

Fig. 7 Significant reduction in the D-gal-induced chronic vascular inflammation and senescence in *Sting*$^{-/-}$ mice. a Schematic diagram of the animal experimental process. Eight-week-old WT and *Sting*$^{-/-}$ mice were subcutaneously injected with an equal amount of D-gal (300 mg·kg^{-1}·d^{-1}) for 8 weeks to induce chronic vascular senescence. **b** The body weights of the mice were weighed on a scale every three days. **c** DHE staining of the frozen aortic sections to detect ROS levels. **d** SA-β-gal staining of the inner layer of the aortas of WT and *Sting*$^{-/-}$ mice ($n = 8$ mice per group). **e** Immunofluorescent staining of STING in the frozen aortic sections of mice. PECAM-1 indicates the endothelial layer. DAPI indicates the cell nucleus. Scale bar: 100 μm. The percentages of STING^{+}PECAM-1^{+} area to PECAM-1^{+} area were calculated ($n = 10$ mice per group). Representative images of immunostaining for p21 (**f**), p53 (**g**), dsDNA (**h**), γ-H2A.X (**i**), p-IRF3 (**j**), and p-NF-κB p65 (**k**) in the aortic endothelium of WT and *Sting*$^{-/-}$ mice. Scale bar: 100 μm. Data were presented as means ± SEM. $^{**}P < 0.01$, $^{***}P < 0.001$, $^{****}P < 0.0001$ was considered significant.

Apoe$^{-/-}$/AAV9-sh*Sting* mice were significantly reduced, while the collagen content was significantly increased compared with the control mice (Fig. 9d–f), indicating that *Sting* depletion in ECs destabilizes atherosclerotic plaques. Western blot analysis of STING expression in ECs and VSMCs isolated from the aorta confirmed the specific knockout of *Sting* in ECs (Fig. 9g). Furthermore, mitochondrial dynamics were determined by measuring the expression of the mitochondrial fission protein DRP1 and the fusion protein MFN2. As shown in Fig. 9i, DRP1 was downregulated, while MFN2 was upregulated in the aortic ECs of *Apoe*$^{-/-}$/AAV9-sh*Sting* mice compared to control mice. In addition, voltage-dependent anion channel (VDAC1), which regulates mtDNA release, was decreased correspondingly, indicating that due to the absence of endothelial *Sting*, the dynamic balance of mitochondrial fusion and fission tends to be stable from fission to fusion (Fig. 9i). Accordingly, ROS levels were also reduced after EC-specific *Sting* knockdown (Fig. 9j). Moreover, EC-specific *Sting* knockdown significantly reduced the levels of p21 and ICAM-1 (Fig. 9k, l), and Western blotting on aortic ECs also showed inflammation-related indicators (ICAM-1, VCAM-1) and STING pathway-related indicators (p-TBK1, p-IRF3, p-NF-κB) and age-related indexes (γ-H2A.X, p53, p21) were significantly decreased (Fig. 9h), indicating that EC-specific *Sting* knockdown significantly alleviated the degree of vascular senescence and inflammation. In addition, total cholesterol (TC), triglyceride (TG), low-density lipoprotein cholesterol (LDL-C), and high-density lipoprotein cholesterol (HDL-C) levels did not differ between *Apoe*$^{-/-}$/AAV9-sh*Sting* mice and *Apoe*$^{-/-}$/AAV9-shControl mice fed with HFD (Supplementary Fig. S11). Collectively, these results suggest that activating endothelial STING signaling promotes the development of atherosclerosis by regulating endothelial senescence, inflammation, and mitochondrial dysfunction.

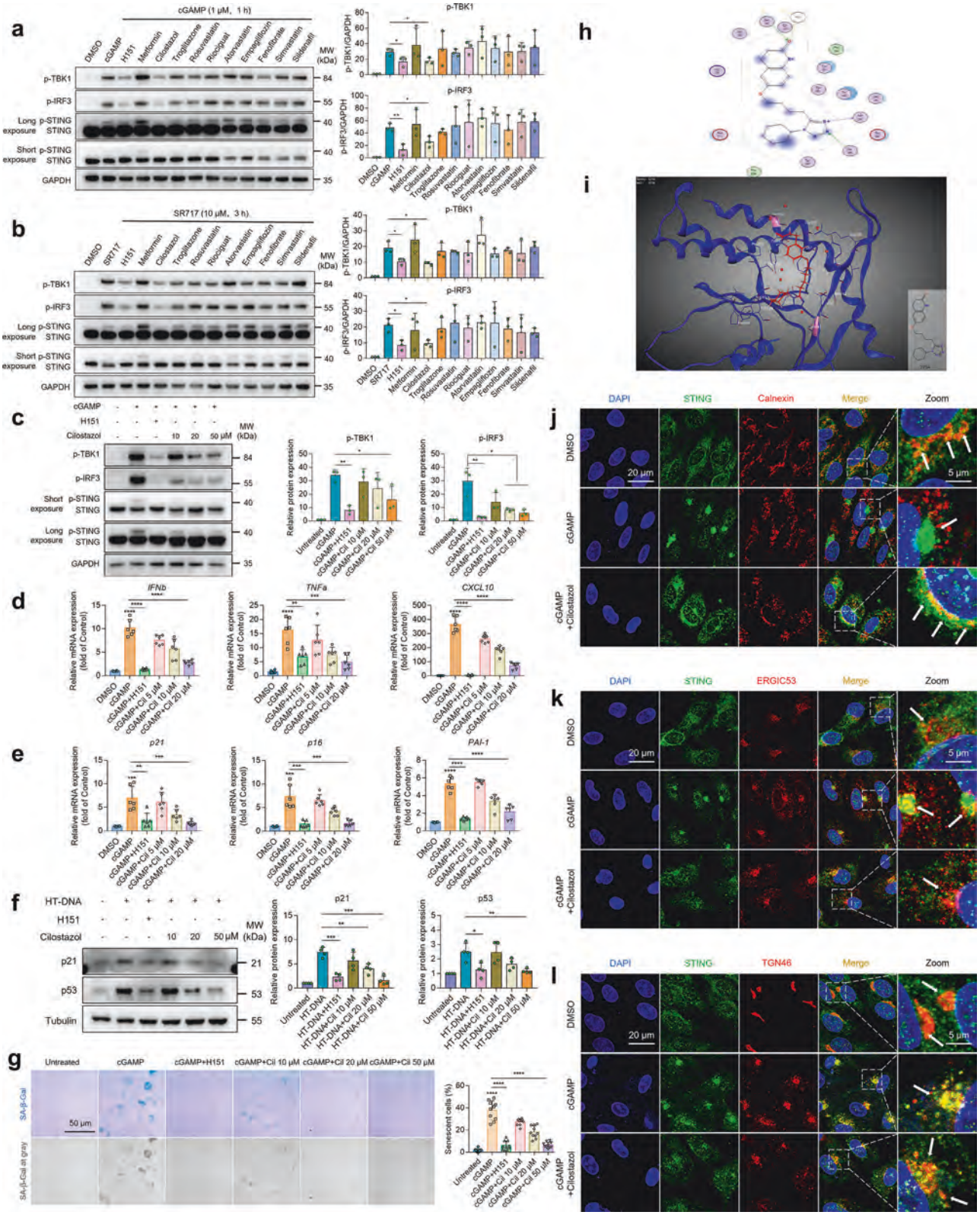

DISCUSSION

Vascular endothelial senescence and associated endothelial inflammation and mitochondrial dysfunction are the common basis of many chronic diseases in the elderly and significantly affect the development and outcome of atherosclerotic CVDs. Thus, it is crucial to identify therapeutic targets to prevent aging-related endothelial inflammation and mitochondrial dysfunction. Recent evidence suggests that the DNA-sensing adapter protein STING is essential for inflammation and macrophage/microglia activation in a variety of diseases, such as vascular diseases [15,

Fig. 8 Identification of Cilostazol as a negative regulator of STING and EC inflammation and senescence induced by STING activation. Effect of selected 10 FDA-approved cardiovascular drugs in our in-house library on the activation of the STING pathway. Immunoblot analysis of the protein levels of STING pathway related indicators (p-TBK1, p-IRF3, p-STING, STING) in HUVECs stimulated with or without cGAMP (1 μM, 1 h) (**a**) or SR717 (10 μM, 3 h) (**b**) in the presence or absence of H151 (10 μM, 12 h) or various candidate drugs (20 μM, 12 h). **c** Immunoblot analysis of protein levels of STING pathway-related indicators in HUVECs stimulated with or without cGAMP (500 nM, 6 h) in the presence or absence of H151 (10 μM, 12 h) or Cilostazol (10, 20, 50 μM, 12 h). **d**, **e** RT-PCR analysis of the indicated genes in HUVECs treated with or without cGAMP (500 nM, 6 h) in the presence or absence of H151 (10 μM, 12 h) or Cilostazol (5, 10, 20 μM, 12 h). **f** Immunoblot analysis of protein levels of p53 and p21 in HUVECs transfected with or without HT-DNA (2 μg/mL) for 24 h in the presence or absence of H151 (10 μM, 12 h) or Cilostazol (10, 20, 50 μM, 12 h). **g** SA-β-gal staining of HUVECs treated as described in (**c**). Scale bar: 50 μm. The quantification of the senescence cell ratio is shown in the right panel. **h, i** Molecular virtual docking is used to analyze the docking degree between the structure of the STING protein and the structure of Cilostazol compounds. **j**–**l** HUVECs were fixed and stained with marker antibodies for the ER (Calnexin, **j**), the ERGIC53 (**k**), and the trans-Golgi network (TGN46, **l**) after being treated with or without cGAMP (1 μM, 1 h) in the presence or absence of Cilostazol (20 μM, 12 h), and images were then captured by confocal microscopy. All images are representative of at least three independent experiments in which >95% of the cells displayed similar staining. Scale bar: 20 μm. Data were presented as means ± SEM from at least three independent experiments. $^{*}P < 0.05$, $^{**}P < 0.01$, $^{***}P < 0.001$, $^{****}P < 0.0001$.

49, 50] and neurodegenerative diseases [51, 52]. However, its role in vascular endothelial senescence has not been well established. In this study, we demonstrated that the STING pathway was activated in diverse trigger-induced EC senescences, including both oxidative stress-induced premature senescence and cell division-induced replicative senescence. Endothelial-specific STING deficiency decreased EC senescence, inflammation, and mitochondrial dysfunction and prevented the development of atherosclerosis in mice. Mechanistically, we demonstrated that the release of dsDNA and mtDNA, respectively derived from nuclear DNA and mitochondrial DNA damage, activates the STING pathway, leading to various SASP factor production to further aggravate ageing-related endothelial inflammation and mitochondrial dysfunction, thus forming a vicious circle (Fig. 10). Importantly, we identified Cilostazol, an FDA-approved vasoprotective drug, as a novel STING inhibitor that alleviates vascular endothelial inflammation and senescence.

The inner layer is the first barrier between blood vessels and blood flow, and EC damage, aging, and dysfunction are considered to be the initiating factors of atherosclerosis [28, 53–55]. Nevertheless, the mechanism of EC senescence has not yet been fully elucidated. At present, factors such as cell cycle disorder, oxidative stress, vascular inflammation, and dysfunction of the renin-angiotensin-aldosterone system have been shown to induce endothelial senescence [56, 57]. Among them, EC senescence induced by telomere erosion and oxidative stress is a crucial factor leading to the decline of endothelial function and age-related CVDs, and both have in common the activation of the DNA damage response, increasing ROS levels, activating the inflammatory system, and causing cell cycle arrest, thus initiating DNA repair or apoptosis procedures [58]. DNA damage, which affects the majority of senescence phenotypes, may be a potential unifying cause of senescence [59]. Studying DNA damage and its mechanistic links with aging phenotypes will provide a rational theoretical basis for developing unified interventions to combat age-related dysfunction and disease. Aging leads to DNA mutations or chromosome aberrations, which lead to genomic instability [60]. With the passage of time, DNA damage inevitably accumulates, making genomic instability an important sign of aging [61, 62]. dsDNA in the cytoplasm, as a damage-related molecular pattern, activates different DNA pattern recognition receptors and induces the innate immune response. STING, a cytosolic DNA sensor that detects the absence of infection by foreign microorganisms, plays a critical role in identifying free DNA released into the cytoplasm due to DNA or mitochondrial damage [15, 63]. Of note, a recent study reported that cigarette smoke extract-induced DNA damage and cytosolic DNA accumulation activated the cGAS-STING pathway, implying that smoking-related DNA damage may cause atherosclerosis in smokers [64]. Therefore, we focused on exploring STING's possible mechanism of action on intracellular DNA damage in senescent ECs and the development of atherosclerosis according to its characteristics as a DNA damage recognition molecule in innate immunity. Through in vivo and in vitro experiments, our study demonstrated that the leakage of free dsDNA and mtDNA into the cytoplasm due to aging stress is the real trigger of STING activation and an inflammatory response aggravating endothelial senescence. Consistent with our findings, a very recent study also showed cGAS/STING signaling could regulate cell senescence and inflammation in early diabetic retinopathy [65]. Senescent ECs further release more cfDNA, thus forming a vicious feedback loop. Interestingly, we found that STING inhibition or knockdown in turn suppressed cfDNA release, supporting the notion that blocking the STING pathway will interrupt the cfDNA-mediated vicious circle and re-establish homeostasis in the senescent vascular tissues. In in vivo studies of both acute and chronic aging, the aortic endothelial senescence phenotype of global *Sting*-deficient mice was alleviated, and the content of free dsDNA in ECs was also significantly decreased. Similar results were obtained when STING was inhibited pharmacologically using C-176. To establish the role of EC-specific STING activation in vascular endothelial senescence in vivo, we also generated endothelial-specific *Sting*-knockdown mice and found that ablation of endothelial *Sting* also ameliorated aortic endothelial senescence and associated endothelial inflammation and mitochondrial dysfunction. These findings indicate that cfDNA-induced overactivation of the STING pathway is a pathogenic mechanism for ageing-related endothelial inflammation and mitochondrial dysfunction.

Previous studies have reported that cytosolic DNA is a key signal for SASP induction. Both mitochondrial dysfunction and persistent DNA damage responses contribute to SASP formation by increasing cytoplasmic DNA formation [66, 67]. Cytoplasmic DNA is perceptive, passing through the cyclic GMP-AMP synthase (cGAS), which then produces cGAMP, activating STING. Nevertheless, whether STING activation induces certain SASP factors in ECs to further worsen EC senescence through feedback has not been established. Intriguingly, our in vitro data demonstrated that, under inflammatory stimuli and other aging pressure, the STING pathway was activated to induce EC senescence and SASP, leading to a large release of cfDNA and STING downstream inflammatory mediators (TNFα and IFNβ), which further exacerbate EC senescence. Furthermore, STING activation exacerbated the effect of oxidative stress-mediated monocyte adhesion to ECs, while STING inhibition significantly alleviated monocyte adhesion under aging conditions. Consistently with the in vitro results, both EC-specific *Sing* knockdown and global *Sting* deficiency significantly reduced cfDNA contents, suppressed the activation of inflammatory pathways under aging pressure, and alleviated endothelial senescence in vivo. Together, these observations indicate that STING activation under endothelial aging pressure induces key SASP factors, such as cfDNA, TNFα, and IFNβ, which act in a feedback loop to reinforce the

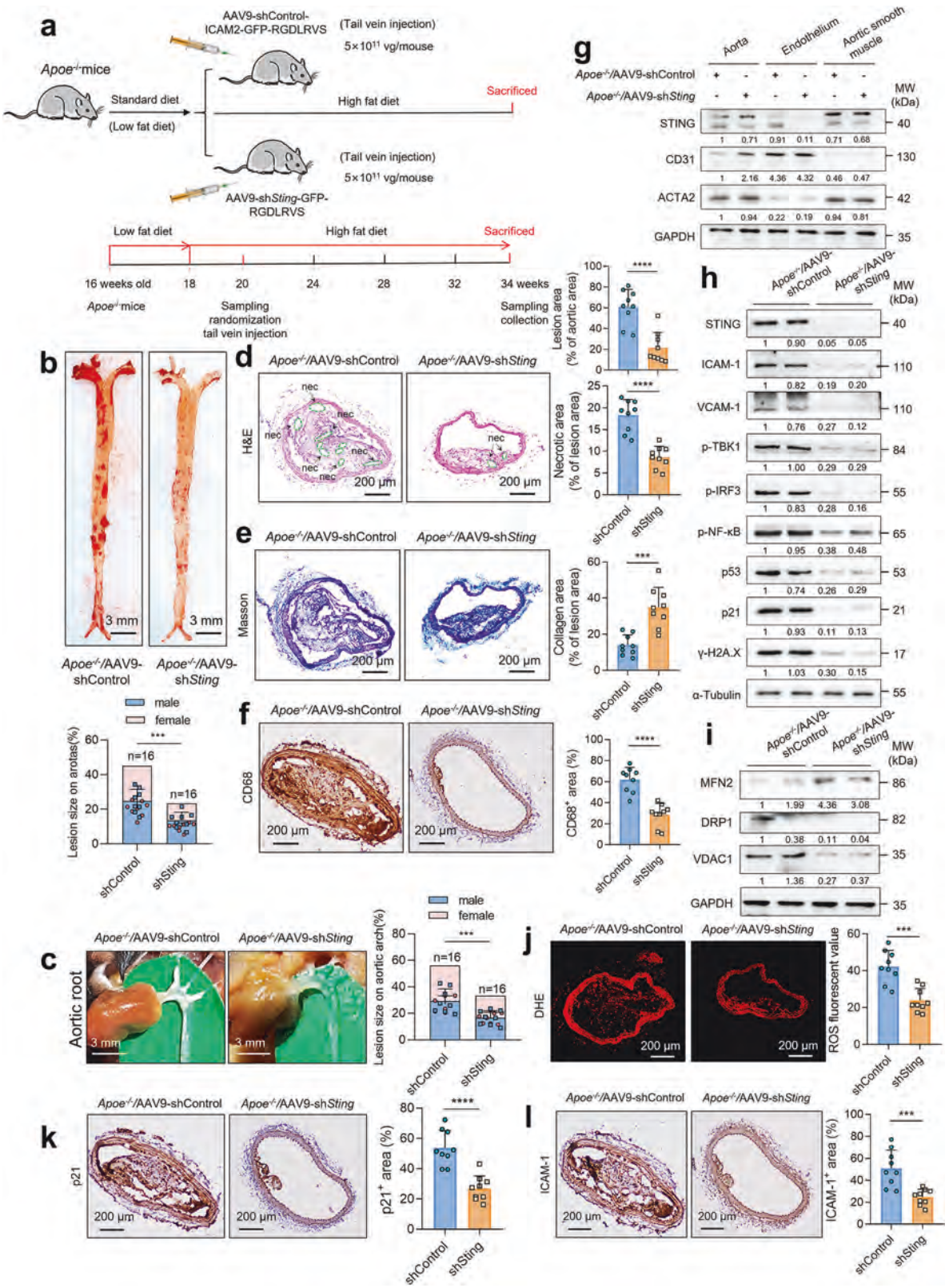

inflammatory effect and amplify the vicious cycle of aging-related endothelial inflammation.

Finally, when STING was selected as the target for drug screening, we discovered that Cilostazol had an inhibitory effect comparable to that of the positive control inhibitor H151. Cilostazol, as a phosphodiesterase type 3 (PDE3) inhibitor approved by the FDA in 1999, has the effects of vasodilation and anti-platelet coagulation, and is currently widely used in the clinical treatment of chronic arterial occlusive disease caused by atherosclerosis, arteritis, thromboangiitis obliterans, and diabetes [68, 69]. However, whether

Fig. 9 EC-specific *Sting* knockdown reduced the development of atherosclerosis in *Apoe*$^{-/-}$ mice. a Schematic diagram of the animal experimental process. **b** Oil red O-stained *en face* aortic preparations from *Apoe*$^{-/-}$/AAV9-shControl and *Apoe*$^{-/-}$/AAV9-sh*Sting* mice fed a Western diet for 16 weeks, and quantification of the Oil red O-stained areas. **c** The aortic arch was dissected and photographed; lesion areas were quantified ($n = 16$ mice per group). **d**, **e** Representative images and quantification data of cross-sections of the aorta brachiocephalic trunk of *Apoe*$^{-/-}$/AAV9-shControl and *Apoe*$^{-/-}$/AAV9-sh*Sting* mice with 16 weeks of Western diet. Sections were stained with hematoxylin and eosin (plaque) and Masson's trichrome (collagen). Scale bar: 200 μm; $n = 9$ mice per group. **f** The protein expression of CD68 in the cross-sections of the aorta brachiocephalic trunk was shown as brown intensity by immunohistochemistry staining. **g** The EC-specific knockdown of *Sting* was verified by Western blot analysis of STING expression in ECs and VSMCs isolated from the aorta. CD31 indicates ECs, and ACTA2 indicates VSMCs. **h** Immunoblot analysis of the protein expression of senescence-related indicators (γ-H2A.X, p21, p53), STING pathway-related indicators (p-TBK1, p-IRF3, p-NF-κB), and vascular inflammation-related indicators (ICAM-1, VCAM-1) in the aortic endothelium from *Apoe*$^{-/-}$/AAV9-shControl and *Apoe*$^{-/-}$/AAV9-sh*Sting* mice ($n = 6$ mice per group). **i** Western blot analysis of MFN2, DRP1, and VDAC1 in ECs of the aorta from *Apoe*$^{-/-}$/AAV9-shControl and *Apoe*$^{-/-}$/AAV9-sh*Sting* mice. $n = 6$ mice per group. **j** The ROS levels of the cross-sections of the aorta brachiocephalic trunk were evaluated by DHE staining. The protein expression of p21 (**k**) and ICAM-1 (**l**) in the cross-sections of the aorta brachiocephalic trunk was shown to have brown intensity by immunohistochemistry staining. Scale bar: 200 μm. Data were presented as means ± SEM. $^{***}P < 0.001$, $^{****}P < 0.0001$ was considered significant.

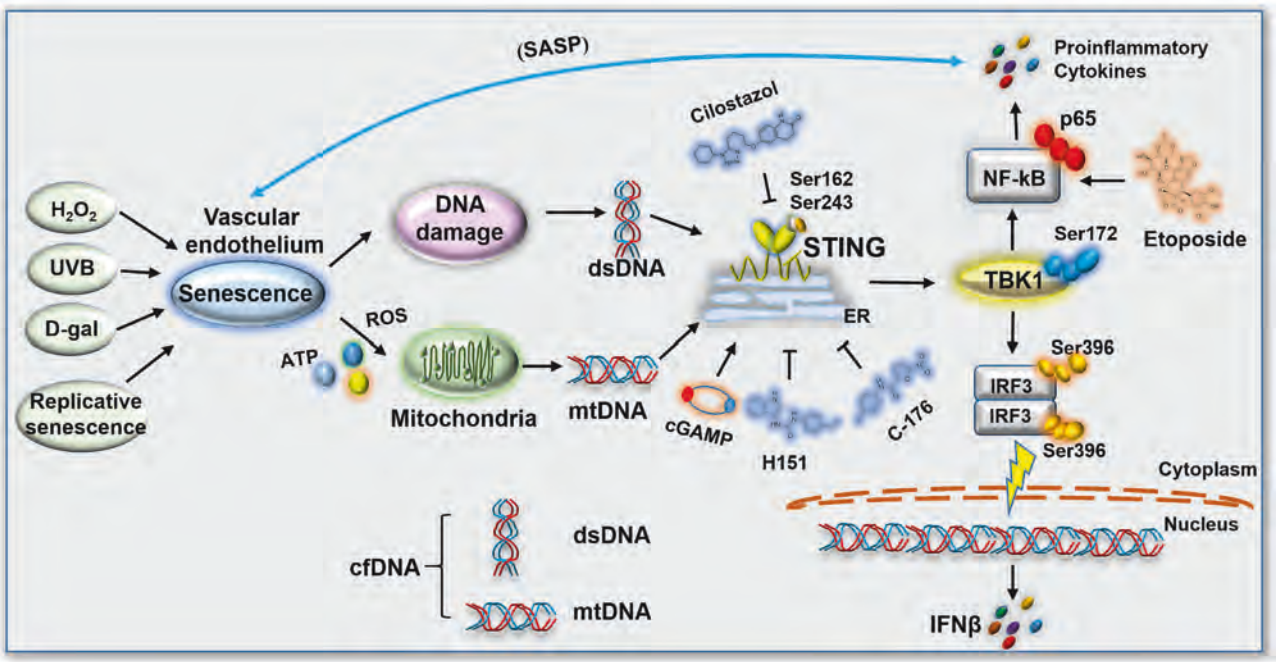

Fig. 10 A proposed model illustrates the central role of STING in mediating a vicious circle of cfDNA-STING-SASP-cfDNA to aggravate age-related endothelial inflammation and mitochondrial damage.

Cilostazol is capable of regulating STING activity in vascular ECs is unknown. We revealed that Cilostazol significantly suppresses the STING pathway by targeting STING's S162 and S243 sites. Moreover, in vivo experiments further confirmed that Cilostazol significantly reduced the vascular endothelial aging phenotype by alleviating aortic ROS levels, downregulating STING expression, attenuating aortic DNA damage, and reducing inflammation in the aortic endothelium (Supplementary Fig. S8). Our study demonstrated that Cilostazol alleviated EC senescence and inflammation by inhibiting STING activation both in vitro and in vivo, providing a feasible therapeutic option for vascular aging-related diseases. Unlike traditional STING inhibitors such as C-176, H151 specifically and effectively labels STING through the formation of covalent bonds between the electrophilic nitrofuran groups of its compounds and STING's nucleophilic Cys91, and then the binding inhibits the palmitoylation process of STING without damaging transport or affecting endolysosomal degradation [39]. Our curiosity lies in how Cilostazol inhibits STING activation. Molecular virtual docking and site-directed mutagenesis showed that Cilostazol targeted STING active sites Ser162 and Ser243, which have been reported to be crucial sites for the binding functions of STING agonists [41–45]. Indeed, our results showed that Cilostazol significantly inhibited STING translocation from the ER to the Golgi apparatus. Therefore, these observations indicate that Cilostazol might act as a competitive inhibitor to affect the binding of STING and agonists.

There are some limitations to this study. Firstly, considering that aging appears to cause greater DNA damage in vascular ECs than VSMCs [4, 5], we focused on the role of STING in vascular ECs. However, STING in other cell types in the vascular microenvironment, such as VSMCs, fibroblasts, macrophages, and other immune cells, may also contribute to vascular aging and inflammation, which warrants further studies. Secondly, in the current study, we used two different aging models: paraquat-induced acute vascular aging and D-gal-induced subacute vascular aging in mice. Further studies are still required to evaluate the effects of STING deletion or inhibition on vascular EC senescence in naturally aging mice. In addition, although HUVECs are widely used by many investigators to study EC function, there may be some differences between HUVECs and other types of ECs, such as human aortic ECs and human coronary artery ECs. Thus, the role of the cfDNA-STING pathway in aging-related endothelial inflammation and mitochondrial dysfunction will need to be verified in other EC types in the future.

In summary, our study suggests that the cytosolic DNA sensing adapter STING is essential for vascular endothelial senescence and aging-related endothelial inflammation, mitochondrial dysfunction, and atherogenesis. Mechanistically, cfDNA release, caused by nuclear DNA and mitochondrial damage under aging stress, induces STING activation, leading to SASP via the NF-κB pathway, which in turn promotes mitochondrial damage and STING activation through feedback, thereby exacerbating vascular endothelial senescence. Therefore, interrupting this pernicious cycle in ECs by inhibiting STING may be an effective strategy for preventing vascular diseases associated with endothelial senescence, such as atherosclerotic CVDs.

ACKNOWLEDGEMENTS

This work is supported by National Natural Science Foundation of China (82270500, 81870324, 82203304, U21A20419), Guangdong Basic and Applied Basic Research Foundation (2024B1515020113), Local Innovative and Research Teams Project of Guangdong Pearl River Talents Program (2017BT01Y093) and National Engineering and Technology Research Center for New Drug Druggability Evaluation (Seed Program of Guangdong Province, 2017B090903004).

AUTHOR CONTRIBUTIONS

ZHZ, PQL, and ZPL designed the study. ZHZ, JJW, JGL, WLY, JMZ, LYL, PLY, WLQ, YYL, SJY, and MZ performed the experiments and analyzed the data. ZHZ wrote the manuscript. QZ, CZL, ML, ZML, DMZ, PQL and ZPL provided the reagents or materials, participated in designing the experiments, and critically reviewed and revised the manuscript.

ADDITIONAL INFORMATION

Supplementary information The online version contains supplementary material available at https://doi.org/10.1038/s41401-024-01281-0.

Competing interests: The authors declare no competing interests.

REFERENCES

1. Harry BL, Sanders JM, Feaver RE, Lansey M, Deem TL, Zarbock A, et al. Endothelial cell PECAM-1 promotes atherosclerotic lesions in areas of disturbed flow in ApoE-deficient mice. Arterioscler Thromb Vasc Biol. 2008;28:2003–8.
2. Alexander Y, Osto E, Schmidt-Trucksäss A, Shechter M, Trifunovic D, Duncker DJ, et al. Endothelial function in cardiovascular medicine: a consensus paper of the European Society of Cardiology Working Groups on Atherosclerosis and Vascular Biology, Aorta and Peripheral Vascular Diseases, Coronary Pathophysiology and Microcirculation, and Thrombosis. Cardiovasc Res. 2021;117:29–42.
3. Luo S, Kong C, Zhao S, Tang X, Wang Y, Zhou X, et al. Endothelial HDAC1-ZEB2-NuRD complex drives aortic aneurysm and dissection through regulation of protein S-sulfhydration. Circulation. 2023;147:1382–403.
4. Muñoz-Espín D, Serrano M. Cellular senescence: from physiology to pathology. Nat Rev Mol Cell Biol. 2014;15:482–96.
5. Abdellatif M, Rainer PP, Sedej S, Kroemer G. Hallmarks of cardiovascular ageing. Nat Rev Cardiol. 2023. https://doi.org/10.1038/s41569-023-00881-3.
6. Xu S, Ilyas I, Little PJ, Li H, Kamato D, Zheng X, et al. Endothelial dysfunction in atherosclerotic cardiovascular diseases and beyond: from mechanism to pharmacotherapies. Pharmacol Rev. 2021;73:924–67.
7. Chi C, Fu H, Li YH, Zhang GY, Zeng FY, Ji QX, et al. Exerkine fibronectin type-III domain-containing protein 5/irisin-enriched extracellular vesicles delay vascular ageing by increasing SIRT6 stability. Eur Heart J. 2022;43:4579–95.
8. Zhang Y, Wang X, Li XK, Lv SJ, Wang HP, Liu Y, et al. Sirtuin 2 deficiency aggravates ageing-induced vascular remodelling in humans and mice. Eur Heart J. 2023;44:2746–59.
9. Takeuchi O, Akira S. Pattern recognition receptors and inflammation. Cell. 2010;140:805–20.
10. Chen Q, Sun L, Chen ZJ. Regulation and function of the cGAS-STING pathway of cytosolic DNA sensing. Nat Immunol. 2016;17:1142–9.
11. Wu B, Xu MM, Fan C, Feng CL, Lu QK, Lu HM, et al. STING inhibitor ameliorates LPS-induced ALI by preventing vascular endothelial cells-mediated immune cells chemotaxis and adhesion. Acta Pharmacol Sin. 2022;43:2055–66.
12. Song J, Yang RR, Chang J, Liu YD, Lu CH, Chen LF, et al. Discovery and characterization of a novel cGAS covalent inhibitor for the treatment of inflammatory bowel disease. Acta Pharmacol Sin. 2023;44:791–800.
13. Oduro PK, Zheng X, Wei J, Yang Y, Wang Y, Zhang H, et al. The cGAS-STING signaling in cardiovascular and metabolic diseases: future novel target option for pharmacotherapy. Acta Pharm Sin B. 2022;12:50–75.
14. Li N, Zhou H, Wu H, Wu Q, Duan M, Deng W, et al. STING-IRF3 contributes to lipopolysaccharide-induced cardiac dysfunction, inflammation, apoptosis and pyroptosis by activating NLRP3. Redox Biol. 2019;24:101215.
15. Pham PT, Fukuda D, Nishimoto S, Kim-Kaneyama JR, Lei XF, Takahashi Y, et al. STING, a cytosolic DNA sensor, plays a critical role in atherogenesis: a link between innate immunity and chronic inflammation caused by lifestyle-related diseases. Eur Heart J. 2021;42:4336–48.
16. Wu X, Yu N, Ye Z, Gu Y, Zhang C, Chen M, et al. Inhibition of cGAS-STING pathway alleviates neuroinflammation-induced retinal ganglion cell death after ischemia/reperfusion injury. Cell Death Dis. 2023;14:615.
17. Wang K, Li Y, Wang X, Zhang Z, Cao L, Fan X, et al. Gas therapy potentiates aggregation-induced emission luminogen-based photoimmunotherapy of poorly immunogenic tumors through cGAS-STING pathway activation. Nat Commun. 2023;14:2950.
18. Luo W, Zou X, Wang Y, Dong Z, Weng X, Pei Z, et al. Critical role of the cGAS-STING pathway in doxorubicin-induced cardiotoxicity. Circ Res. 2023;132:e223–42.
19. Arévalo Martínez M, Ritsvall O, Bastrup JA, Celik S, Jakobsson G, Daoud F, et al. Vascular smooth muscle-specific YAP/TAZ deletion triggers aneurysm development in mouse aorta. JCI insight. 2023;8:e170845.
20. Takahashi A, Loo TM, Okada R, Kamachi F, Watanabe Y, Wakita M, et al. Downregulation of cytoplasmic DNases is implicated in cytoplasmic DNA accumulation and SASP in senescent cells. Nat Commun. 2018;9:1249.
21. Zhang L, Pitcher LE, Yousefzadeh MJ, Niedernhofer LJ, Robbins PD, Zhu Y. Cellular senescence: a key therapeutic target in aging and diseases. J Clin Invest. 2022;132:e158450.
22. Zu Y, Liu L, Lee MY, Xu C, Liang Y, Man RY, et al. SIRT1 promotes proliferation and prevents senescence through targeting LKB1 in primary porcine aortic endothelial cells. Circ Res. 2010;106:1384–93.
23. Lee OH, Woo YM, Moon S, Lee J, Park H, Jang H, et al. Sirtuin 6 deficiency induces endothelial cell senescence via downregulation of forkhead box M1 expression. Aging. 2020;12:20946–67.
24. Luo W, Li J, Li Z, Lin T, Zhang L, Yang W, et al. HO-1 nuclear accumulation and interaction with NPM1 protect against stress-induced endothelial senescence independent of its enzymatic activity. Cell Death Dis. 2021;12:738.
25. Garcez ML, de Carvalho CA, Mina F, Bellettini-Santos T, Schiavo GL, da Silva S, et al. Sodium butyrate improves memory and modulates the activity of histone deacetylases in aged rats after the administration of d-galactose. Exp Gerontol. 2018;113:209–17.
26. Yang Q, Xu J, Ma Q, Liu Z, Sudhahar V, Cao Y, et al. PRKAA1/AMPKα1-driven glycolysis in endothelial cells exposed to disturbed flow protects against atherosclerosis. Nat Commun. 2018;9:4667.
27. Xu Y, Wang Y, Yan S, Yang Q, Zhou Y, Zeng X, et al. Regulation of endothelial intracellular adenosine via adenosine kinase epigenetically modulates vascular inflammation. Nat Commun. 2017;8:943.
28. Wang J, Liu Z, Lu J, Zou J, Ye W, Li H, et al. SIRT6 regulates endothelium-dependent relaxation by modulating nitric oxide synthase 3 (NOS3). Biochem Pharmacol. 2023;209:115439.
29. Zhang L, Liu M, Liu W, Hu C, Li H, Deng J, et al. Th17/IL-17 induces endothelial cell senescence via activation of NF-κB/p53/Rb signaling pathway. Lab Invest. 2021;101:1418–26.
30. Wu Y, Tang L, Huang H, Yu Q, Hu B, Wang G, et al. Phosphoglycerate dehydrogenase activates PKM2 to phosphorylate histone H3T11 and attenuate cellular senescence. Nat Commun. 2023;14:1323.
31. Zeng JP, Bi B, Chen L, Yang P, Guo Y, Zhou YQ, et al. Repeated exposure of mouse dermal fibroblasts at a sub-cytotoxic dose of UVB leads to premature senescence: a robust model of cellular photoaging. J Dermatol Sci. 2014;73:49–56.
32. Permatasari F, Hu YY, Zhang JA, Zhou BR, Luo D. Anti-photoaging potential of Botulinum Toxin Type A in UVB-induced premature senescence of human dermal fibroblasts in vitro through decreasing senescence-related proteins. J Photochem Photobiol B. 2014;133:115–23.
33. Kakimoto PA, Serna JDC, de Miranda Ramos V, Zorzano A, Kowaltowski AJ. Increased glycolysis is an early consequence of palmitate lipotoxicity mediated by redox signaling. Redox Biol. 2021;45:102026.
34. Zhou M, Diwu Z, Panchuk-Voloshina N, Haugland RP. A stable nonfluorescent derivative of resorufin for the fluorometric determination of trace hydrogen peroxide: applications in detecting the activity of phagocyte NADPH oxidase and other oxidases. Anal Biochem. 1997;253:162–8.
35. Ogrodnik M. Cellular aging beyond cellular senescence: markers of senescence prior to cell cycle arrest in vitro and in vivo. Aging Cell. 2021;20:e13338.
36. Chao T, Shih HT, Hsu SC, Chen PJ, Fan YS, Jeng YM, et al. Autophagy restricts mitochondrial DNA damage-induced release of ENDOG (endonuclease G) to regulate genome stability. Autophagy. 2021;17:3444–60.

37. Yum S, Li M, Fang Y, Chen ZJ. TBK1 recruitment to STING activates both IRF3 and NF-κB that mediate immune defense against tumors and viral infections. Proc Natl Acad Sci USA. 2021;118:e2100225118.
38. Dunphy G, Flannery SM, Almine JF, Connolly DJ, Paulus C, Jønsson KL, et al. Non-canonical activation of the DNA sensing adaptor STING by ATM and IFI16 mediates NF-κB signaling after nuclear DNA damage. Mol Cell. 2018;71:745–60.e5.
39. Haag SM, Gulen MF, Reymond L, Gibelin A, Abrami L, Decout A, et al. Targeting STING with covalent small-molecule inhibitors. Nature. 2018;559:269–73.
40. Chin EN, Yu C, Vartabedian VF, Jia Y, Kumar M, Gamo AM, et al. Antitumor activity of a systemic STING-activating non-nucleotide cGAMP mimetic. Science. 2020;369:993–9.
41. Gao P, Ascano M, Zillinger T, Wang W, Dai P, Serganov AA, et al. Structure-function analysis of STING activation by c[G(2′,5′)pA(3′,5′)p] and targeting by antiviral DMXAA. Cell. 2013;154:748–62.
42. Zhang X, Shi H, Wu J, Zhang X, Sun L, Chen C, et al. Cyclic GMP-AMP containing mixed phosphodiester linkages is an endogenous high-affinity ligand for STING. Mol Cell. 2013;51:226–35.
43. Ramanjulu JM, Pesiridis GS, Yang J, Concha N, Singhaus R, Zhang SY, et al. Design of amidobenzimidazole STING receptor agonists with systemic activity. Nature. 2018;564:439–43.
44. Huang YH, Liu XY, Du XX, Jiang ZF, Su XD. The structural basis for the sensing and binding of cyclic di-GMP by STING. Nat Struct Mol Biol. 2012;19:728–30.
45. Stazzoni S, Böhmer DFR, Hernichel F, Özdemir D, Pappa A, Drexler D, et al. Novel poxin stable cGAMP-derivatives are remarkable STING agonists. Angew Chem (Int ed Engl). 2022;61:e202207175.
46. Hansen AL, Buchan GJ, Rühl M, Mukai K, Salvatore SR, Ogawa E, et al. Nitro-fatty acids are formed in response to virus infection and are potent inhibitors of STING palmitoylation and signaling. Proc Natl Acad Sci USA. 2018;115:E7768–e75.
47. Zhang BC, Nandakumar R, Reinert LS, Huang J, Laustsen A, Gao ZL, et al. STEEP mediates STING ER exit and activation of signaling. Nat Immunol. 2020;21:868–79.
48. Motani K, Saito-Tarashima N, Nishino K, Yamauchi S, Minakawa N, Kosako H. The Golgi-resident protein ACBD3 concentrates STING at ER-Golgi contact sites to drive export from the ER. Cell Rep. 2022;41:111868.
49. Luo W, Wang Y, Zhang L, Ren P, Zhang C, Li Y, et al. Critical role of cytosolic DNA and its sensing adaptor STING in aortic degeneration, dissection, and rupture. Circulation. 2020;141:42–66.
50. Ma X, Wu W, Liang W, Takahashi Y, Cai J, Ma JX. Modulation of cGAS-STING signaling by PPARalpha in a mouse model of ischemia-induced retinopathy. Proc Natl Acad Sci USA. 2022;119:e2208934119.
51. Gulen MF, Samson N, Keller A, Schwabenland M, Liu C, Gluck S, et al. cGAS-STING drives ageing-related inflammation and neurodegeneration. Nature. 2023;620:374–80.
52. Xie X, Ma G, Li X, Zhao J, Zhao Z, Zeng J. Activation of innate immune cGAS-STING pathway contributes to Alzheimer's pathogenesis in 5xFAD mice. Nat Aging. 2023;3:202–12.
53. Wang JC, Bennett M. Aging and atherosclerosis: mechanisms, functional consequences, and potential therapeutics for cellular senescence. Circ Res. 2012;111:245–59.
54. Tyrrell DJ, Goldstein DR. Ageing and atherosclerosis: vascular intrinsic and extrinsic factors and potential role of IL-6. Nat Rev Cardiol. 2021;18:58–68.
55. Xiao X, Jiang H, Wei H, Zhou Y, Ji X, Zhou C. Endothelial senescence in neurological diseases. Aging Dis. 2023;14:2153–66.
56. Jia G, Aroor AR, Jia C, Sowers JR. Endothelial cell senescence in aging-related vascular dysfunction. Biochim Biophys Acta Mol Basis Dis. 2019;1865:1802–9.
57. Vanhoutte PM, Shimokawa H, Feletou M, Tang EH. Endothelial dysfunction and vascular disease—a 30th anniversary update. Acta Physiol. 2017;219:22–96.
58. Jazayeri A, Falck J, Lukas C, Bartek J, Smith GC, Lukas J, et al. ATM- and cell cycle-dependent regulation of ATR in response to DNA double-strand breaks. Nat Cell Biol. 2006;8:37–45.
59. Di Micco R, Krizhanovsky V, Baker D, d'Adda di Fagagna F. Cellular senescence in ageing: from mechanisms to therapeutic opportunities. Nat Rev Mol Cell Biol. 2021;22:75–95.
60. López-Otín C, Blasco MA, Partridge L, Serrano M, Kroemer G. Hallmarks of aging: an expanding universe. Cell. 2023;186:243–78.
61. Zhao Y, Simon M, Seluanov A, Gorbunova V. DNA damage and repair in age-related inflammation. Nat Rev Immunol. 2023;23:75–89.
62. Guo J, Huang X, Dou L, Yan M, Shen T, Tang W, et al. Aging and aging-related diseases: from molecular mechanisms to interventions and treatments. Signal Transduct Target Ther. 2022;7:391.
63. Wu X, Wu FH, Wang X, Wang L, Siedow JN, Zhang W, et al. Molecular evolutionary and structural analysis of the cytosolic DNA sensor cGAS and STING. Nucleic Acids Res. 2014;42:8243–57.
64. Ueda K, Sakai C, Ishida T, Morita K, Kobayashi Y, Horikoshi Y, et al. Cigarette smoke induces mitochondrial DNA damage and activates cGAS-STING pathway: application to a biomarker for atherosclerosis. Clin Sci. 2023;137:163–80.
65. Liu H, Ghosh S, Vaidya T, Bammidi S, Huang C, Shang P, et al. Activated cGAS/STING signaling elicits endothelial cell senescence in early diabetic retinopathy. JCI insight. 2023;8:e168945.
66. Vizioli MG, Liu T, Miller KN, Robertson NA, Gilroy K, Lagnado AB, et al. Mitochondria-to-nucleus retrograde signaling drives formation of cytoplasmic chromatin and inflammation in senescence. Genes Dev. 2020;34:428–45.
67. Correia-Melo C, Marques FD, Anderson R, Hewitt G, Hewitt R, Cole J, et al. Mitochondria are required for pro-ageing features of the senescent phenotype. EMBO J. 2016;35:724–42.
68. de Havenon A, Sheth KN, Madsen TE, Johnston KC, Turan TN, Toyoda K, et al. Cilostazol for secondary stroke prevention: history, evidence, limitations, and possibilities. Stroke. 2021;52:e635–e45.
69. Schaler AW, Myeku N. Cilostazol, a phosphodiesterase 3 inhibitor, activates proteasome-mediated proteolysis and attenuates tauopathy and cognitive decline. Transl Res. 2018;193:31–41.